processes

MDPI

Article

Study on Minimum Miscibility Pressure of CO_2–Oil System in Deep High-Temperature and High-Pressure Reservoirs

Hong-Mei Wang [1], Li-Jian Li [1], Hong Chen [2], Wei Xiong [3,4,*], Ye Tian [3], Yu-Long Zhao [3], Yu-Jia Zeng [1] and Xian-Yu Jiang [3]

[1] Exploration and Development Research Institute, PetroChina Huabei Oilfield Company, Renqiu 062552, China
[2] PetroChina Huabei Oilfield Company, Renqiu 062552, China
[3] National State Key Laboratory of Oil and Gas Reservoir Geology and Exploitation, Southwest Petroleum University, Chengdu 610500, China
[4] Institute of Marine Natural Gas Hydrates, Southwest Petroleum University, Chengdu 610500, China
* Correspondence: wei.xiong@swpu.edu.cn

Abstract

Deep high-temperature and high-pressure (HTHP) oil reservoirs have limited experimental MMP data, large differences between reservoir and saturation pressures, low gas–oil ratios, and pressure-sensitive CO_2–oil phase behavior, which make both minimum miscibility pressure (MMP) prediction and miscibility-mechanism identification challenging. To address these gaps, this study determines the MMP of a CO_2–oil system by integrating slim-tube experiments, empirical formula methods, the Multiple Mixed-Cell (MMC) method, the Method of Characteristics (MOC), compositional numerical simulation, and three intelligent algorithm models (GWO-RBF, GWO-LSSVM, and GWO-SVM). The slim-tube MMP of 44.13 MPa at 140 °C is used as the experimental reference for comparing prediction errors, whereas PVTsim and literature data are used for consistency checks and model benchmarking. The results show that when the injected CO_2 mole fraction exceeds 0.88, the formation oil under original reservoir conditions cannot achieve first-contact miscibility with CO_2, and the maximum dissolved CO_2–oil molar ratio is 7.3:1. Supercritical CO_2 forms dual displacement mechanisms, including front-end vaporizing miscible drive and rear-end condensing miscible drive, but the dominant mechanism for this CO_2–oil system is vaporizing miscible drive. During the vaporizing gas drive, the $CO_2 + N_2 + C_1$ content in the liquid phase increases from less than 60% to nearly 90%, indicating significant CO_2 dissolution into oil and associated density and viscosity reduction; meanwhile, the C_{7+} content in the gas phase increases to nearly 10%, indicating extraction of heavy components. Relative to the slim-tube reference at 140 °C, the deviations of MMC, GWO-SVM, GWO-LSSVM, compositional numerical simulation, GWO-RBF, MOC, and empirical formula methods are 2.97%, 3.08%, 3.40%, 4.24%, 4.26%, 11.62%, and 19.74%, respectively. The MMC method is the most suitable approach for this specific HTHP oil system, while intelligent algorithms should be regarded as supplementary predictors whose reliability depends on training-domain coverage and independent validation.

Keywords: high-temperature and high-pressure reservoirs; minimum miscibility pressure; slim-tube test; Multiple Mixed-Cell method; intelligent algorithm

Check for updates

Academic Editor: Chuanjin Yao

Received: 2 June 2026
Revised: 18 June 2026
Accepted: 23 June 2026
Published: 25 June 2026

Copyright: © 2026 by the authors. Licensee MDPI, Basel, Switzerland. This article is an open access article distributed under the terms and conditions of the Creative Commons Attribution (CC BY) license.

1. Introduction

CO_2 injection into deep HTHP oil reservoirs can enhance oil recovery and support CO_2 storage, but reliable MMP data remain scarce under ultra-deep, high-temperature,

and high-pressure conditions [1]. The target reservoir is buried at 4200 to 5800 m, with pressures of 51.28 to 58.63 MPa and temperatures of 133.3 to 149.7 °C. Its high pour point (35 to 53 °C), low gas–oil ratio, large reservoir-pressure/saturation-pressure difference, heavy composition (MWC_{7+} = 381.48 g/mol), and low C_2–C_6 mole fraction (7.5% to 14.8%) make CO_2 miscibility strongly pressure- and composition-dependent. Figure 1 and Table 1 show that most published CO_2–oil MMP data are from lower-temperature, lower-pressure, and lighter-oil systems; therefore, the measured MMP of 44.13 MPa represents a relatively high HTHP case that requires method-specific interpretation of the controlling miscibility mechanism.

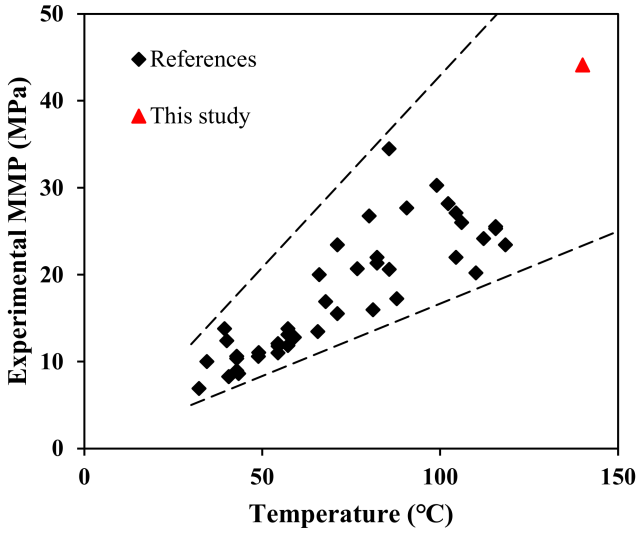


Figure 1. Statistical chart of MMP experimental measurements and reservoir temperature.

Table 1. Statistical table of CO_2–oil MMP experimental measurements.

References	T_R (°C)	x_{vol} (%)	$x_{int'}$ (%)	x_{int} (%)	MWC_{5+} (g/mol)	MWC_{7+} (g/mol)	MMP (MPa)
Holm and Josendal [2]	54.40~87.80	0~31.80	1.57~5.11	9.30~16.90	170.50~182.60	178.00~197.00	12.07~17.24
Alston et al. [3]	67.80~112.20	31.00~53.36	2.95~35.64	3.00~36.00	180.60~240.70	185.00~245.00	16.90~30.27
Rathmell et al. [4]	39.40~85.60	17.07~44.53	18.34~21.81	22.30~30.03	199.70~247.80	222.00~268.00	10.35~34.49
Jaubert et al. [5]	104.40	38.80	14.58	19.65	285.00	327.00	27.10
Zuo et al. [6]	85.65	17.36	12.92	32.19	276.00	282.00	20.61
Eakin and Mitch [7]	82.22~115.56	6.74~32.99	20.59~42.44	27.50~47.42	188.00~263.00	216.00~281.00	21.34~25.54
Sun et al. [8]	66.00~106.00	24.15~25.01	7.89~11.53	11.54~13.80	225.00~391.00	233.00~402.70	20.00~26.00
Graue and Zana [9]	71.10	4.40	13.90	24.68	207.90	227.94	15.52
Dicharry et al. [10]	54.40	29.48	31.82	40.05	171.20	197.40	11.00
Gardner et al. [11]	42.80	19.35	26.80	33.12	196.10	221.00	10.62
Thakur et al. [12]	118.33	34.94	27.53	33.64	172.00	190.00	23.44
Metcalfe [13]	32.20~65.60	10.50~34.34	14.28~22.82	24.44~26.39	187.25~187.77	200.0~206.00	6.90~13.45
Dong et al. [14]	59.00	5.45	11.35	18.93	205.00	220.00	12.80
Shelton and Yarborough [15]	34.40	16.78	10.76	17.70	212.56	227.00	10.00
Henry and Metcalfe [16]	48.90	12.50	22.62	31.00	205.10	227.00	10.59
Khan et al. [17]	40.56~43.33	7.31~9.01	25.22~26.67	31.74~36.86	207.00~218.00	229.00~248.00	8.27~8.62
Chaback et al. [18]	54.44~104.44	9.82~42.71	5.17~29.43	7.58~37.32	154.00~218.00	173.00~224.00	11.78~21.99
Spence and Watkins [19]	40.00~42.80	17.04~24.25	17.24~23.85	23.42~30.71	202.00~221.00	221.00~235.00	8.96~12.4
Al-Ajmi et al. [20]	90.56	40.08	18.76	24.31	232.00	256.14	27.68
This study	140.00	8.95	5.63	10.03	365.81	381.48	44.13

Note: T_R is the reservoir temperature (°C); x_{vol} is the sum of the mole fractions of N_2 and CH_4 (%); $x_{int'}$ is the sum of the mole fractions of CO_2, H_2S, and C_2–C_4 (%); x_{int} is the sum of the mole fractions of CO_2, H_2S, and C_2–C_6 (%); MWC_{5+} is the molecular weight of C_{5+} (g/mol); MW_{C7+} is the molecular weight of C_{7+} (g/mol). The commonly used CO_2–oil MMP methods include empirical correlations, MMC, MOC, numerical simulation, and intelligent algorithms. Empirical correlations use experimental regressions based on temperature, oil composition, and injected-gas composition. Representative formulas by Cronquist [21], Lee et al. [22], Alston et al. [3], and Li et al. [23] are computationally efficient, and the Li et al. correlation improves prediction for oils rich in C_{7+} by using TR, x_{vol}, xC_2–C_6, and MWC_{7+}. However, such formulas are mainly suitable for rapid screening and may lose accuracy outside their calibration range.

MMC methods simulate sequential vapor–liquid equilibria with thermodynamic models to describe vaporizing, condensing, and combined multiple-contact miscibility (Figure 2). Previous work showed that CO_2 concentration, slim-tube displacement behavior, and front-end vaporizing/rear-end condensing contact processes all affect MMP estimates [24–26]. For HTHP oils with heavy fractions, the main issue is not only the calculated pressure value but also which mass-transfer path controls miscibility as pressure increases.

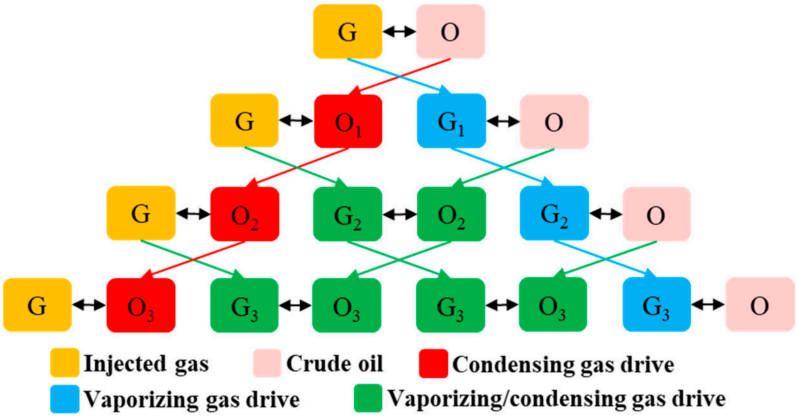


Figure 2. Schematic diagram of multiple contacts for the Multiple Mixed-Cell method.

The MOC estimates CO_2–oil MMP from one-dimensional flow and tie-line analysis. It identifies the initial oil tie-line, injection-gas tie-line, and intermediate crossover tie-lines along the compositional route. Yang et al. [27,28] developed analytical tie-line calculations and examined the influence of C_4, C_{10}, C_{14}, and C_{20} fractions, while Wang [29] noted that calculated results still require validation. Thus, MOC offers efficient trend screening, but its simplifying assumptions must be checked for heavy-component HTHP fluids.

Intelligent algorithms predict CO_2–oil MMP by learning nonlinear relationships among reservoir temperature, fluid composition, injected-gas composition, and measured MMP. Models such as Multilayer perceptron (MLP), Genetic algorithm-radial basis function model (GA-RBF), Random forest (RF), Particle swarm optimization–gradient boosting decision tree model (PSO-GBDT), Adaptive boosting support vector regression (AdaBoost SVR), GA-based models, and modified mayfly–MLP models have reported good prediction performance [30–32]. However, their generalization depends strongly on the coverage and independence of training samples, which remains a key constraint for HTHP reservoirs with limited experimental data.

These studies leave three connected gaps: limited experimental MMP evidence for deep HTHP medium oils, insufficient linkage between prediction error and vaporizing/condensing mass transfer, and limited separation between experimental validation and thermodynamic-model consistency in data-driven modeling. This work addresses these gaps by applying slim-tube benchmarking, PR-EoS model, multiple-contact mechanism analysis, numerical simulation, and intelligent algorithms to the same HTHP oil system.

Therefore, this study aims to determine the CO_2–oil MMP, identify the dominant miscibility mechanism, and define the applicable scenarios and limitations of experimental, analytical, numerical, and intelligent prediction methods for similar deep HTHP reservoirs.

2. Methodology

To improve the logical hierarchy, the methodology is organized into three categories: experimental methods for fluid characterization and slim-tube MMP measurement; classical analytical and numerical methods, including empirical correlations, MMC, MOC, compositional simulation, and the PR equation of state; and intelligent prediction meth-

ods, including GWO-RBF, GWO-LSSVM, and GWO-SVM. The compared methods were selected to cover a direct experimental benchmark, empirical screening, thermodynamic multiple-contact calculation, analytical tie-line calculation, flow-coupled numerical simulation, and data-driven prediction. The basic equations retained in the main text define the assumptions and implementation variables required for reproducibility, while detailed intelligent-algorithm formulations are provided in the Supplementary Materials.

2.1. Classical Analytical and Numerical Methods

2.1.1. Empirical Formula

Li et al. [23] modified the expression proposed by Alston et al. [3] by adopting TR, x_{vol}, xC$_2$–C$_6$, and MWC$_{7+}$ as key parameters. This modification enhanced the calculation accuracy for reservoir fluids enriched with heavy C$_{7+}$ components. The established empirical correlation for the CO$_2$–oil MMP is given by

$$\mathrm{MMP} = 7.30991 \times 10^{-5}\left[\ln(1.8T_R + 32)\right]^{5.33647}\left[\ln\left(MW_{C_{7+}}\right)\right]^{2.08836}\left(1 + \frac{x_{\mathrm{vol}}}{x_{\mathrm{int}}}\right)^{0.201658} \quad (1)$$

where MMP is the minimum miscibility pressure (MPa); T_R represents the reservoir temperature (°C); x_{vol} is the sum of the mole fractions of N$_2$ and CH$_4$ (%); x_{int} is the sum of the mole fractions of CO$_2$, H$_2$S, and C$_2$–C$_6$ (%); MWC_{5+} is the molecular weight of C$_{5+}$ (g/mol); MWC_{7+} is the molecular weight of C$_{7+}$ (g/mol).

2.1.2. Multiple Mixing-Cell

The MMC method determines the CO$_2$–oil MMP by simulating the multiple-contact process of the injected gas and reservoir hydrocarbons. This method integrates the tie-line analysis approach to ascertain the achievement of miscibility. The component tie-line length can be calculated by

$$l_i = \sqrt{(x_i - y_i)^2} \quad (2)$$

where l_i is the tie-line length of component i (mol/mol); x_i is the liquid-phase mole fraction of component i (mol/mol); and y_i is the vapor-phase mole fraction of component i (mol/mol).

The MMC method encompasses the vaporizing gas drive, condensing gas drive, and vaporizing/condensing gas drive (Figure 2). The solution workflows for the three processes are illustrated in Figure 3. Computationally, the negative flash [27] calculation method is used to perform flash calculation. The vaporizing gas drive evaluates whether the equilibrium vapor-phase composition is identical to that of the previous contact cycle. The condensing gas drive assesses the equilibrium liquid-phase composition against the previous cycle. The vaporizing/condensing gas drive simultaneously compares both the equilibrium vapor and liquid phases with their respective compositions from the prior cycle. The numerical algorithm proceeds through the following sequential stages:

(1) Input the oil composition, injected gas composition, and reservoir temperature, and set the initial pressure to 1 MPa.
(2) Assume a liquid-phase fraction of 0.5, and calculate the global mixture composition.
(3) Perform negative flash calculations utilizing the Peng–Robinson (PR) [33] EoS to determine the phase-split compositions at vapor–liquid equilibrium.
(4) Calculate the tie-line length for each component using Equation (2), and sum them to obtain the total tie-line length. If the total tie-line length is less than 10^{-4}, the injected gas and crude oil have achieved miscibility, and the calculation terminates; otherwise, proceed to the next step.

(5) Evaluate whether the vapor/liquid phase composition matches that of the previous contact cycle. If identical, increase the pressure and return to step (2); otherwise, increment the number of contacts and return to step (3).

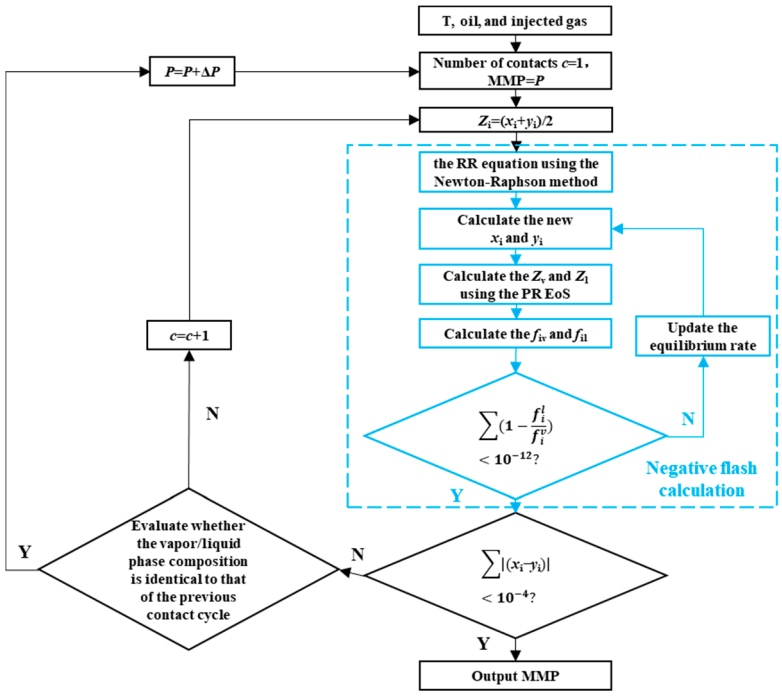


Figure 3. Flowchart of the solving process for the Multiple Mixed-Cell method (RR equation = Rachford–Rice equation; PR EoS = Peng–Robinson equation of state).

2.1.3. Method of Characteristics

The MOC determines the MMP of a CO_2–oil system by analytically solving the one-dimensional flow equation. This method is predicated on the following assumptions: (a) the porous medium is incompressible; (b) the oil–gas system maintains thermodynamic equilibrium throughout the flow process; (c) the pressure gradient variation across the entire system is negligible; (d) capillary and gravity forces are negligible; (e) the temperature remains constant, and the flow is linear; (f) diffusion and dispersion are negligible; and (g) the volume remains constant during the interphase mass transfer of components. The simplified mass conservation equation [34] is expressed as

$$\frac{\partial C_i}{\partial t} + \frac{\partial F_i}{\partial \xi} = 0 \tag{3}$$

where t is the dimensionless time; ζ is the dimensionless distance; C_i is the overall volume fraction of component i; and F_i is the overall flux fraction of component i.

The analytical expressions for the total volumetric fraction and total flux fraction are

$$C_i = c_{i,l}[1 + (K_i - 1)S] \tag{4}$$

$$F_i = c_{i,l}[1 + (K_i - 1)f] \tag{5}$$

where $c_{i,l}$ is the liquid-phase volume fraction of component i; S is the gas saturation; K_i is the equilibrium constant of component i; and f is the gas-phase flux fraction.

The mass conservation equation governing the tie-line is

$$C_i = c_{i,l}(1 - S) + c_{i,v}S \tag{6}$$

where $c_{i,v}$ is the vapor-phase volume fraction of component i.

Combining Equations (2) and (6), the equilibrium constant is defined as

$$K_i = \frac{c_{i,\mathrm{v}}}{c_{i,\mathrm{l}}} \tag{7}$$

The equilibrium compositions must satisfy the normalization condition:

$$\sum_i c_{i,\mathrm{v}} = \sum_i c_{i,\mathrm{l}} = 1 \tag{8}$$

Wang et al. [34] modified the negative flash algorithm:

$$F(c_{1,\mathrm{l}}) = \sum_i \frac{C_i c_{1,\mathrm{l}}(K_1 - 1)(K_i - 1)}{(K_i - 1)C_1 + c_{1,\mathrm{l}}(K_1 - K_i)} = 0 \tag{9}$$

Equation (9) is solved using Newton's method, with the specific steps as follows:

(1) Set the initial value of $c_{1,\mathrm{l}}$ to 0.5, and calculate $F(c_{1,\mathrm{l}})$ based on the current equilibrium constant.

(2) Evaluate whether $|F(c_{1,\mathrm{l}})|$ is less than 10^{-6}. If satisfied, the calculation terminates; otherwise, the procedure moves forward.

(3) Calculate the derivative of $F(c_{1,\mathrm{l}})$ with respect to $c_{1,\mathrm{l}}$ using the following formula:

$$F(c_{1,\mathrm{l}})' = \sum_i \frac{C_i(K_1 - 1)(K_i - 1)}{(K_i - 1)C_1 + c_{1,\mathrm{l}}(K_1 - K_i)} - \sum_i \frac{C_i c_{1,\mathrm{l}}(K_1 - 1)(K_i - 1)(K_1 - K_i)}{[(K_i - 1)C_1 + c_{1,\mathrm{l}}(K_1 - K_i)]^2} \tag{10}$$

(4) Update $c_{1,\mathrm{l}}$ using Newton's iteration:

$$c_{1,\mathrm{l}}{}^{\mathrm{new}} = c_{1,\mathrm{l}}{}^{\mathrm{old}} - \frac{F(c_{1,\mathrm{l}})}{F(c_{1,\mathrm{l}})'} \tag{11}$$

(5) Recalculate $F(c_{1,\mathrm{l}})$ using the updated $c_{1,\mathrm{l}}$ and return to step (2).

After determining $c_{1,\mathrm{l}}$ via Equation (9), calculate S and $c_{\mathrm{i,l}}$ using Equation (4).

Based on the theory of partial differential equations, two adjacent key tie-lines intersect within the phase diagram space. Assuming that component j disappears on crossover tie-line n:

$$C_j = c_{j,\mathrm{l}}{}^n\left[1 + \left(K_j{}^n - 1\right)S^n\right] = 0 \tag{12}$$

The gas saturation on the crossover tie-line n is

$$S^n = \frac{1}{1 - K_j{}^n} \tag{13}$$

Combining Equations (12) and (13) yield

$$C_i = c_{i,\mathrm{l}}{}^n\left(\frac{K_i{}^n - K_j{}^n}{1 - K_j{}^n}\right), i \neq j \tag{14}$$

An adapted negative flash algorithm is utilized to identify the subsequent critical tie-line linked to the crossover node. The key tie-line is defined as

$$l^n = \sqrt{\sum_i \left(c_{i,\mathrm{l}}{}^n - c_{i,\mathrm{v}}{}^n\right)^2} \tag{15}$$

The solution workflow for the MOC is mapped out in Figure 4, with the specific calculation steps as follows:

(1) Set a sufficiently low initial pressure.
(2) Perform the negative flash calculation phase equilibrium to obtain the oil and gas tie-line.
(3) Calculate the composition of the next key tie-line using Equation (14) and the crossover tie-line.
(4) Verify the generation of all requisite key tie-lines. If incomplete, loop back to the second stage; once the entire set of tie-lines is resolved, advance to the final evaluation.
(5) Determine every key tie-line using Equation (15). The computation halts when any length reaches zero (indicating full miscibility); otherwise, increase the pressure and return to step (2).

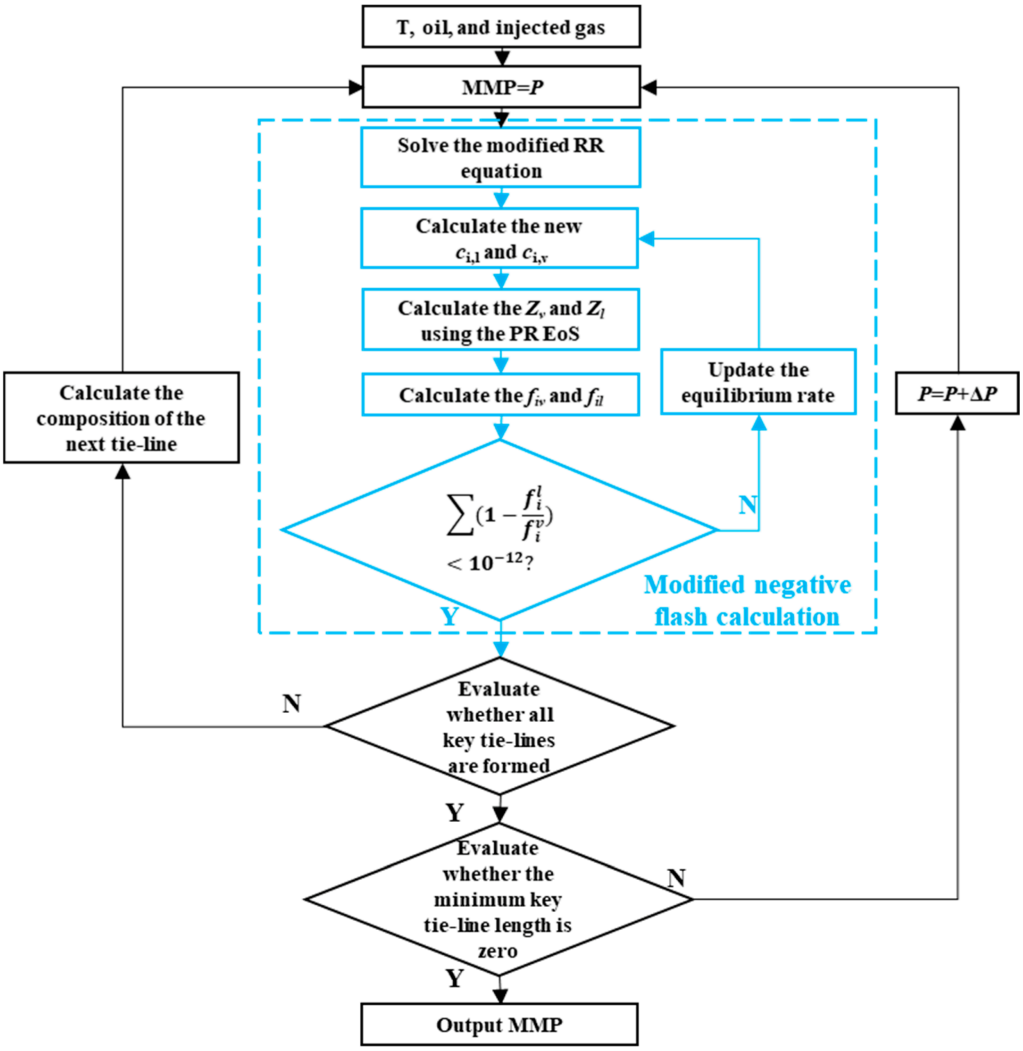


Figure 4. Flowchart of the solving process for the Method of Characteristics.

2.1.4. Numerical Simulation Method

The permeability in slim-tube experiments ranges from 2 to 5 D; thus, the fluid flow within the slim tube is dominated by convection, and diffusion effects can be neglected. The mass conservation equation [35] is defined as

$$\partial_t \left[\phi \sum_{\alpha=l,v} \rho_\alpha S_\alpha X_\alpha^i \right] + \sum_{\alpha=l,v} \nabla \cdot \left(\rho_\alpha X_\alpha^i \overline{v}_\alpha \right) - \sum_{\alpha=l,v} \left(\frac{\rho_\alpha q_\alpha X_\alpha^i}{V_r} \right) = 0 \quad (16)$$

where ϕ is the porosity; ρ_α is the density of phase α (kg/m^3); S_α is the saturation of phase α; $X_{\alpha i}$ is the mass fraction of component i in phase α; v_α is the Darcy seepage velocity of phase α (m/s); q_α is the volumetric flow rate of phase α (m^3/s); and V_r is the volume (m^3).

Convection within the matrix is calculated using Darcy's law

$$\overline{v}_\alpha = \frac{K_d k_{r,\alpha}}{\mu_\alpha}(\nabla p - \gamma g \nabla H) \tag{17}$$

where K_d is the absolute permeability (m^2); μ_α is the viscosity of phase α (Pa·s); p is the pressure (Pa); k_r is the relative permeability; γ is the mass density of the mixture (kg/m^3); g is the acceleration due to gravity (m/s^2); and H is the vertical distance (m).

Xiong et al. [36] proposed fully coupled and semi-coupled models integrating the equation of state (EoS) with flow equations. The detailed coupling procedure is provided in Ref. [36] and will not be reiterated here.

2.1.5. Peng–Robinson Equation of State

Fluid properties are calculated using the PR [33] EoS:

$$p = \frac{RT}{v-b} - \frac{a(T)}{v(v+b)+b(v-b)} \tag{18}$$

where R is the universal gas constant (8.314 J/(mol·K)); T is the temperature (K); v is the molar volume (cm^3/mol); and $a(T)$ and b are the parameters of the PR EoS.

a(T) is the energy parameter of the PR EoS [33]:

$$a = 0.457235\frac{(RT_\mathrm{c})^2}{P_\mathrm{c}}\left[1 + m\left(1 - \sqrt{\frac{T}{T_c}}\right)\right]^2 \tag{19}$$

$$b = 0.077796\frac{RT_\mathrm{c}}{P_\mathrm{c}} \tag{20}$$

$$m = \begin{cases} 0.37464 + 1.54226\omega - 0.26992\omega^2 & \omega \le 0.49 \\ 0.379642 + 1.48503\omega - 0.164423\omega^2 + 0.016666\omega^3 & \omega > 0.49 \end{cases} \tag{21}$$

where P_c is the critical pressure (Pa); T_c is the critical temperature (K); and ω is the acentric factor.

The van der Waals (vdW) mixing rules are employed to calculate the EoS parameters a and b for the mixture:

$$a = \sum_i \sum_j y^i y^j \sqrt{a^i a^j}\left(1 - k^{ij}\right) \tag{22}$$

$$b = \sum_i y^i b^i \tag{23}$$

where k_{ij} is the binary interaction parameter between components i and j.

The PR EoS was selected because it is widely used for compositional CO_2–oil phase-behavior calculations and can be calibrated with the CCE and differential liberation data available in this study. Representative association and electrolyte-association EoS studies provide useful references for modeling confined fluids, CO_2–H_2O, CO_2–CH_4, CO_2–CH_4–H_2O, CCS brines, and CCUS fluids [37–39]. A full sensitivity comparison with alternative equations of state, such as SRK, CPA/eCPA, electrolyte-association, or other association-type EoS models [37–40], was not performed here; this uncertainty is acknowledged as a limitation and should be evaluated when additional HTHP experimental data become available.

2.2. Intelligent Prediction Methods

(1) Radial basis function (RBF) neural network model

The RBF neural network [41] consists of neurons, connection weights between neurons, bias values, and a transfer function (radial basis function) (see Figure 5). Input information is received by neurons in the input layer and transmitted to the hidden layer. The neurons in the hidden layer transform the information via the transfer function and transmit it to the output layer to calculate the predicted value. The RBF neural network employs the Euclidean distance as the basis function and the Gaussian function as the transfer function. It can effectively approximate any local optimum, offering the advantages of multi-parameter nonlinear fitting, rapid local optimization, and adaptive learning. The procedure for constructing the RBF model is outlined below: (a) set the Gaussian function as the radial basis function, and determine its data center and width; (b) establish the RBF neural network structure and train the network, gradually optimizing the network structural parameters using a trial-and-error method; and (c) utilize the RBF model for prediction. The detailed equations of the RBF neural network are proposed in the Supplementary Materials.

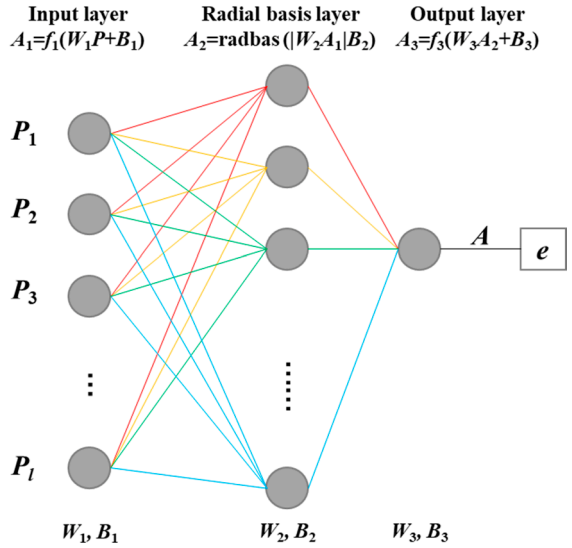


Figure 5. RBF neural network model structure diagram.

(2) Support vector machine (SVM) and least squares support vector machine (LSSVM)

Cortes and Vapnik [42] introduced the fundamental SVM framework, which resolves initial nonlinear regression tasks by nonlinearly projecting datasets into a high-dimensional topological space, thereby enabling linear classification. Functioning as an advanced variant, the LSSVM builds upon the standard SVM by retaining its structural risk minimization paradigm and leveraging the kernel trick to elevate the target problem into an expanded feature dimension. The penalty factor γ and the kernel function width $\sigma 2$ of the LSSVM model are the two parameters that most significantly affect its predictive performance. In this study, the gray wolf optimizer (GWO) is employed to optimize the parameters, γ and $\sigma 2$. The detailed equations of the SVM and LSSVM are proposed in the Supplementary Materials.

(3) Gray wolf optimizer (GWO)

Mirjalili et al. [43] proposed the GWO, a heuristic optimization algorithm that achieves parameter optimization by simulating the predatory behaviors of gray wolves, including tracking, encircling, pursuing, and attacking prey. The GWO exhibits robust global search capabilities and features the advantages of a simple theoretical framework and few parameters. The GWO divides the wolf pack into four social hierarchies: the optimal candidate

solution is assigned the role of α; the subsequent two runner-up agents are categorized as β and δ, respectively, while the rest of the population constitutes the ω group. The optimization process of the GWO is as follows: (a) initialize the population; (b) evaluate the objective function, subsequently assigning the α, β, and δ roles to the three most optimal solutions; (c) determine the prey's location (the global optimal solution) based on the α, β, and δ wolves, while the remaining individuals update their positions relative to the positions of α, β, and δ; and (d) update the algorithm parameters, evaluate whether the wolf pack should search for the next target or continue the attack, and ultimately capture the prey. The detailed equations of the GWO are proposed in the Supplementary Materials.

The GWO is utilized to optimize the RBF, SVM, and LSSVM models, thereby establishing the GWO-RBF, GWO-SVM, and GWO-LSSVM models, respectively. As diagrammed in Figure 6, the proposed numerical framework is executed via the sequence detailed below: (a) initialize the entire wolf pack; (b) calculate the fitness of individual wolves and categorize the pack into α, β, and δ hierarchies based on these fitness values; (c) execute hunting according to the algorithm rules and update the relevant parameters; if the constraint conditions are not met, repeat steps (b) and (c) until the constraints are satisfied; and (d) construct the new RBF, SVM, and LSSVM models for prediction using the optimized parameters.

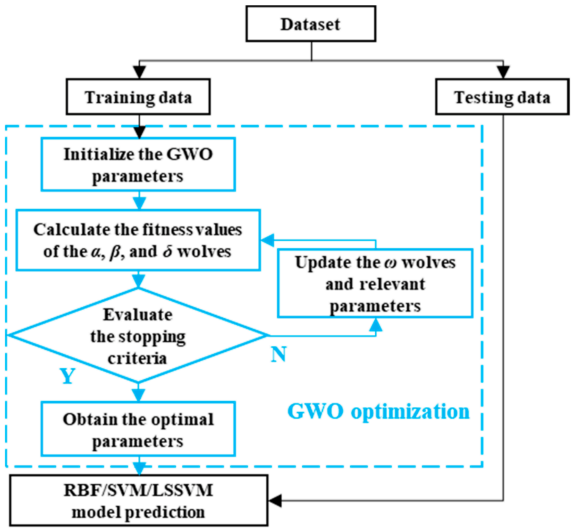


Figure 6. Flowchart of GWO optimizing RBF/SVM/LSSVM (GWO = gray wolf optimizer; RBF = radial basis function; SVM = support vector machine; LSSVM = least-squares support vector machine).

3. Experimental Methods and Fluid Phase Behavior Analysis

3.1. Constant Composition Expansion Experiment

An HTHP fluid analyzer is employed to conduct the constant composition expansion (CCE) experiment. The experimental apparatus, as illustrated in Figure 7, comprises a pressure-volume-temperature (PVT) cell, high-precision pumps, sensors, a flash separator, a gas chromatograph, a constant-temperature system, a control system, and a video recording system. The experimental procedure strictly adhered to the oil and gas industry standard GB/T 26981-2020 [44].

The experimental sample is an oil well-stream sample from a deep-to-ultra-deep HTHP oil reservoir in China. The initial reservoir temperature is 140 °C, and the initial reservoir pressure is 57.05 MPa. The experimental temperature is 140 °C, the saturation pressure is determined to be 3.38 MPa, and the density of the formation oil at the saturation pressure was 0.7974 g/cm^3.

The oil well-stream sample was obtained from the target deep-to-ultra-deep HTHP reservoir and preserved in a sealed high-pressure sampling cylinder before laboratory

testing. Before the CCE experiment, the sample was restored to the reservoir temperature and pressure conditions, homogenized in the PVT cell, and stabilized until no visible phase separation was observed. The CCE test was then conducted by stepwise pressure depletion at 140 °C, with pressure, volume, density, and compressibility recorded after stabilization at each pressure step. The CCE experimental data are shown in Table 2.

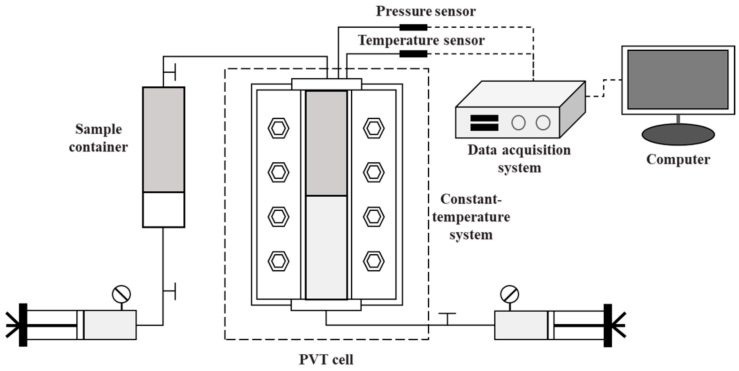


Figure 7. HTHP fluid analyzer.

Table 2. Experimental data of constant component expansion.

Pressure (MPa)	Relative Volume V_i/V_b	Oil Density (g/cm^3)	Compressibility Coefficient (MPa^{-1})
60.00	0.9466	0.8424	5.85×10^{-4}
57.05 *	0.9484	0.8408	6.26×10^{-4}
55.00	0.9496	0.8397	6.54×10^{-4}
50.00	0.9529	0.8368	7.23×10^{-4}
45.00	0.9566	0.8336	7.90×10^{-4}
40.00	0.9605	0.8302	8.57×10^{-4}
35.00	0.9648	0.8265	9.23×10^{-4}
30.00	0.9694	0.8226	9.88×10^{-4}
25.00	0.9743	0.8184	1.05×10^{-3}
20.00	0.9796	0.8140	1.12×10^{-3}
15.00	0.9852	0.8094	1.18×10^{-3}
10.00	0.9911	0.8046	1.24×10^{-3}
5.00	0.9973	0.7996	1.30×10^{-3}
3.38 **	1.0000	0.7974	1.32×10^{-3}
3.36	1.0015		
3.34	1.0024		
3.29	1.0055		
3.23	1.0101		
3.14	1.0167		
3.02	1.0269		
2.75	1.0560		
2.43	1.1051		
2.13	1.1731		
1.86	1.2665		

* Formation pressure; ** bubble-point pressure.

The composition of the oil well-stream is split and lumped. By utilizing the experimental data from saturation pressure, constant composition expansion, and differential liberation tests, the critical parameters of the oil (Table 3) and the binary interaction parameters of the PR EoS (Table 4) are determined through WINPROP of CMG (CMG 2022.10, Computer Modelling Group Ltd., Calgary, AB, Canada) [45].

Table 3. Critical parameters of fluid.

Components	Mole Fraction (%)	*MW* (g/mol)	T_c (K)	P_c (bar)	ω	V_c (dm_3/mol)
N_2	0.58	28.01	126.20	33.50	0.04	0.09
CO_2	1.68	44.01	304.20	72.80	0.23	0.09
C_1	8.37	16.04	190.60	45.40	0.01	0.10
C_2	1.01	30.07	305.40	48.20	0.10	0.15
C_3	0.55	44.10	369.80	41.90	0.15	0.20
iC_4	0.95	58.12	408.10	36.00	0.18	0.26
nC_4	1.44	58.12	425.20	37.50	0.19	0.26
iC_5	1.34	72.15	460.40	33.40	0.23	0.31
nC_5	1.44	72.15	469.60	33.30	0.25	0.30
C_6	1.62	86.00	507.50	32.46	0.28	0.34
C_7–C_9	8.58	106.66	568.46	29.17	0.35	0.42
C_{10}–C_{16}	23.70	177.80	684.89	20.38	0.57	0.68
C_{17}–C_{27}	25.46	306.66	809.01	13.08	0.89	1.11
C_{28}–C_{34}	10.08	411.04	952.25	7.58	1.29	1.46
C_{35}–C_{36}	13.19	1048.07	823.24	6.92	1.47	2.73

Table 4. Binary interaction parameters.

	N_2	CO_2	C_1	C_2	C_3	iC_4	nC_4	iC_5	nC_5	C_6	C_7–C_9	C_{10}–C_{16}	C_{17}–C_{27}	C_{28}–C_{34}	C_{35}–C_{36}
N_2	0	0	0.025	0.010	0.090	0.095	0.095	0.100	0.110	0.110	0.110	0.110	0.110	0.110	0.000
CO_2	0	0	0.105	0.130	0.125	0.120	0.115	0.115	0.115	0.115	0.115	0.115	0.115	0.115	0.075
C_1	0.025	0.105	0	0.003	0.009	0.016	0.015	0.021	0.021	0.025	0.034	0.059	0.091	0.110	0.158
C_2	0.010	0.130	0.003	0	0.002	0.005	0.005	0.009	0.009	0.012	0.018	0.037	0.064	0.082	0.126
C_3	0.090	0.125	0.009	0.002	0	0.001	0.001	0.003	0.003	0.005	0.009	0.024	0.046	0.062	0.102
iC_4	0.095	0.120	0.016	0.005	0.001	0	0.000	0.000	0.000	0.001	0.004	0.015	0.034	0.047	0.084
nC_4	0.095	0.115	0.015	0.005	0.001	0.000	0	0.001	0.001	0.001	0.004	0.016	0.035	0.049	0.086
iC_5	0.100	0.115	0.021	0.009	0.003	0.000	0.001	0	0.000	0.000	0.002	0.010	0.027	0.039	0.074
nC_5	0.110	0.115	0.021	0.009	0.003	0.000	0.001	0.000	0	0.000	0.002	0.011	0.027	0.040	0.074
C_6	0.110	0.115	0.025	0.012	0.005	0.001	0.001	0.000	0.000	0	0.001	0.008	0.023	0.034	0.066
C_7–C_9	0.110	0.115	0.034	0.018	0.009	0.004	0.004	0.002	0.002	0.001	0	0.004	0.016	0.025	0.055
C_{10}–C_{16}	0.110	0.115	0.059	0.037	0.024	0.015	0.016	0.010	0.011	0.008	0.004	0	0.004	0.010	0.030
C_{17}–C_{27}	0.110	0.115	0.091	0.064	0.046	0.034	0.035	0.027	0.027	0.023	0.016	0.004	0	0.001	0.013
C_{28}–C_{34}	0.110	0.115	0.110	0.082	0.062	0.047	0.049	0.039	0.040	0.034	0.025	0.010	0.001	0	0.006
C_{35}–C_{36}	0.000	0.075	0.158	0.126	0.102	0.084	0.086	0.074	0.074	0.066	0.055	0.030	0.013	0.006	0

Figure 8 presents the fitting results of the CCE experiment. Utilizing the PR EoS parameters from Tables 3 and 4, the variations in the relative volume, density, and viscosity of the formation crude oil with pressure are accurately predicted, yielding average absolute relative deviations of 0.90%, 0.23%, and 2.49%, respectively.

3.2. CO_2–Oil First-Contact Miscibility Pressure

Figure 9a displays the PT phase diagram of the oil. Under the specified formation temperature, the saturation pressure of the initial fluid evaluates to 3.38 MPa. The crude oil remains in a single-phase state at the reservoir pressure. When extracted to surface conditions, it enters the two-phase region, releasing a small amount of gas. Figure 9b illustrates the phase diagrams of the crude oil mixed with different injected CO_2 molar fractions. As the injected CO_2 molar fraction increases, the single-phase region gradually

shrinks. When the injected CO_2 molar fraction reaches 0.88, the single-phase region (liquid-phase region) disappears. The first-contact miscibility pressure represents the specific condition where the injected fluid and oil can completely dissolve into a single miscible phase when mixed in any proportion. Because the formation crude oil and CO_2 remain in a two-phase state at any pressure when the injected CO_2 molar fraction exceeds 0.88, the formation crude oil and CO_2 cannot achieve first-contact miscibility. However, a maximum CO_2 solubility exists; when the reservoir pressure exceeds 52.1 MPa, 0.12 mol of crude oil can dissolve a maximum of 0.88 mol of CO_2 (crude oil:CO_2 = 1:7.3 mol/mol).

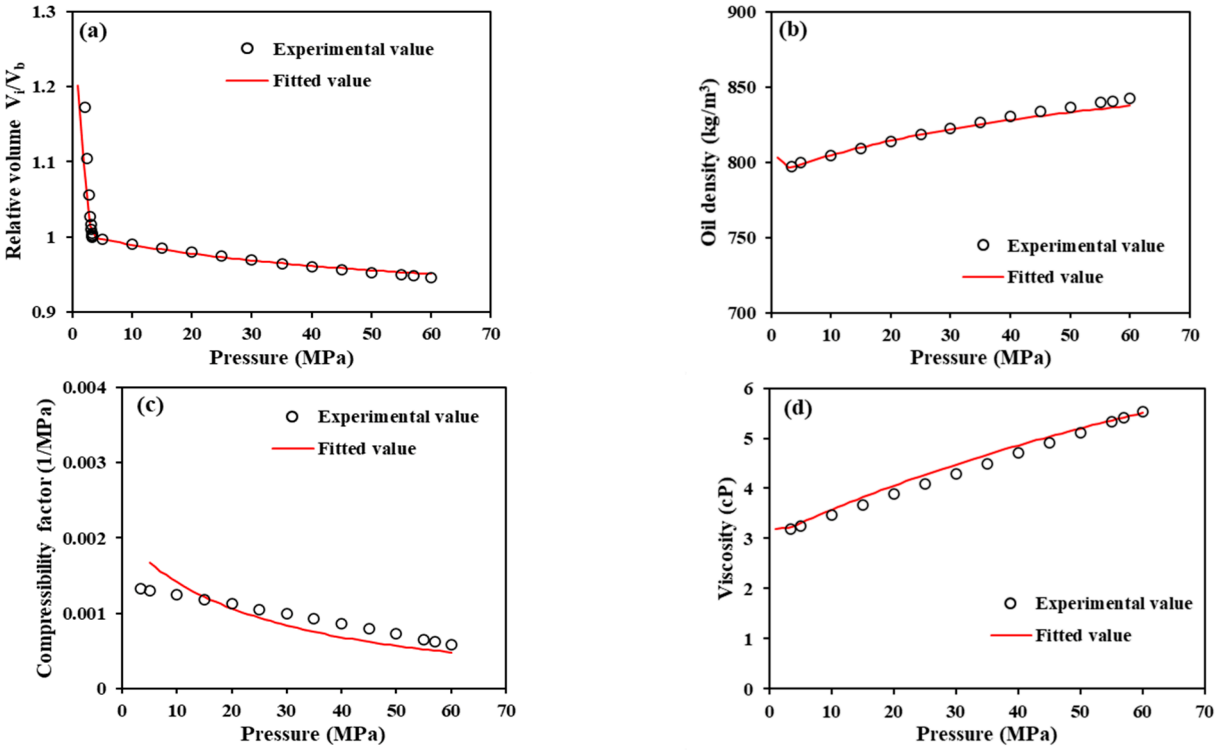


Figure 8. Relative volume vs. pressure (**a**); density vs. pressure (**b**); compression coefficient vs. pressure (**c**); viscosity vs. pressure (**d**).

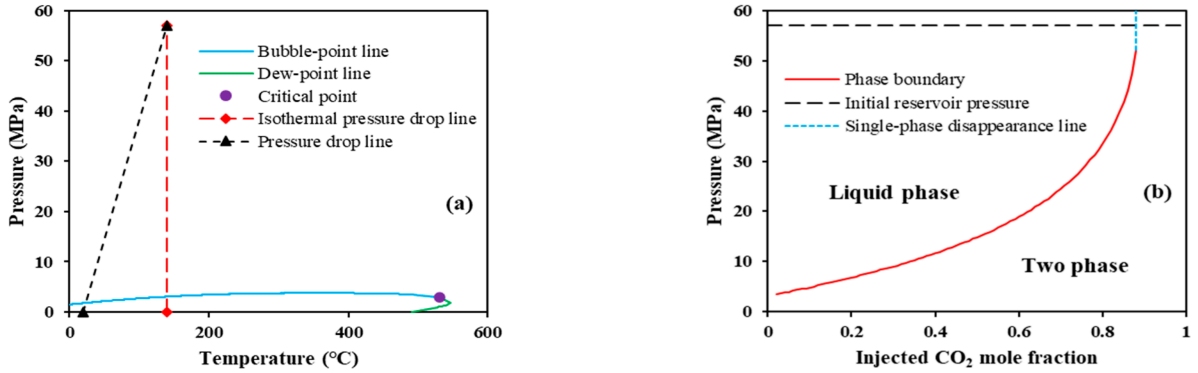


Figure 9. PT phase diagram (**a**); pressure vs. injected CO_2 phase diagram (**b**).

Figure 10 presents the variations in the liquid-phase CO_2 molar fraction, liquid-phase deviation factor, liquid-phase density, and viscosity with pressure. As shown in Figure 10a, the CO_2 solubility in the liquid phase increases with an increasing injected CO_2 molar fraction. As the pressure increases, the CO_2 solubility increases within the two-phase region, whereas it remains constant in the single-phase region (where the CO_2 solubility exceeds the CO_2 supply). With increasing pressure, the CO_2 solubility increases rapidly

at low pressures, while it increases slowly at high pressures. Figure 10c illustrates that liquid density drops in the low-pressure two-phase regime due to the solubility of CO_2 within the oil phase. Conversely, in the high-pressure single-phase region, the oil density increases as the pressure rises. According to the trends in Figure 10d, the viscosity of the crude oil decreases as the CO_2 content increases. The calculation results demonstrate that CO_2 injection can effectively reduce the density and viscosity of the crude oil. At native formation conditions, the density is reduced by 3.29%, and the viscosity is reduced by 82.05%.

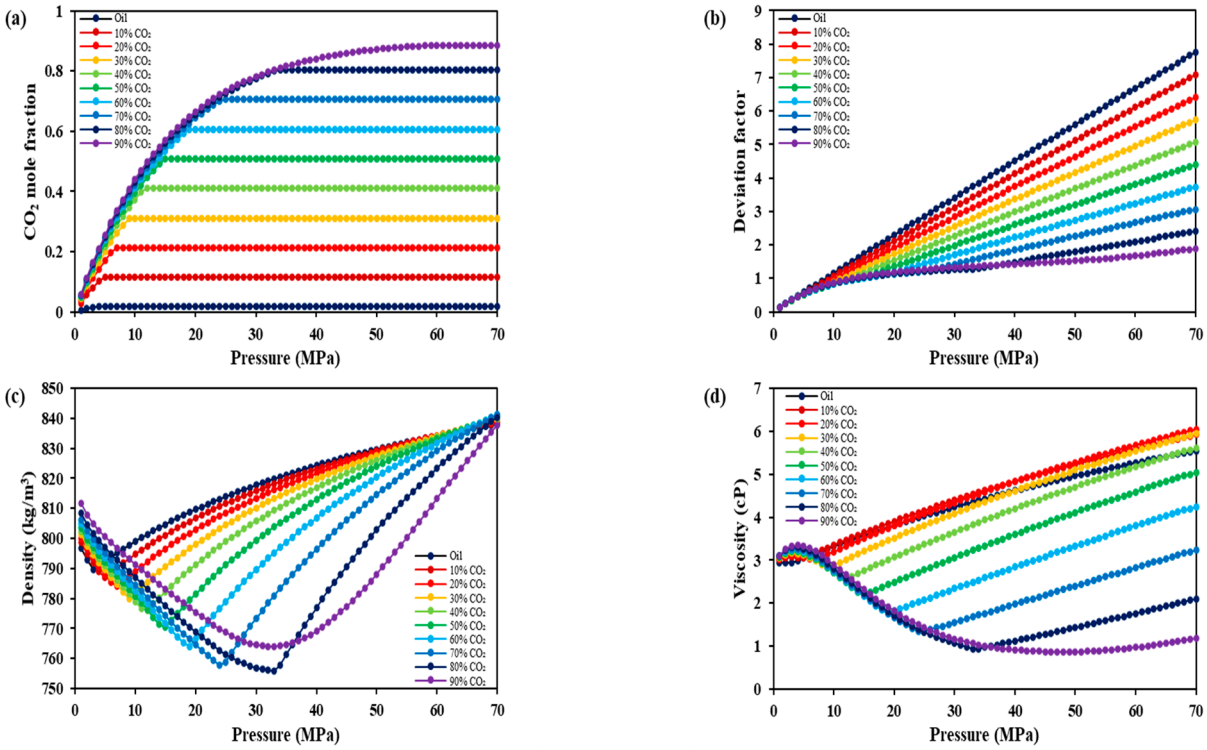


Figure 10. Molar fraction vs. pressure (**a**); deviation factor vs. pressure (**b**); density vs. pressure (**c**); viscosity vs. pressure (**d**).

3.3. CO_2–Oil Minimum Miscibility Pressure Experiment

The experimental evaluation of the CO_2–oil MMP is achieved through a slim-tube displacement test. Figure 11 illustrates the schematic diagram of the experimental apparatus, which comprises a displacement unit, a constant-temperature system, a back-pressure system, a metering unit, and high-precision pumps. The slim-tube method was selected as the reference method because it directly captures dynamic multiple-contact miscibility during continuous CO_2 displacement and is commonly used to benchmark analytical, numerical, and data-driven MMP predictions. The experimental procedure strictly adhered to the oil and gas industry standard SY/T 5542-2009 [46].

The experimental temperature is 140 °C, and the testing pressures are set at 36, 42, 46, 50, and 53 MPa. To evaluate repeatability, at least three test runs were conducted in both immiscible and miscible displacement regimes. The measured MMP of 44.13 MPa falls between the 42 and 46 MPa displacement tests; therefore, the pressure-step-based experimental uncertainty is estimated as ±2.0 MPa, corresponding to approximately ±4.5% of the measured MMP. Subsequently, the correlation between pressure and CO_2 flooding recovery efficiency after injecting 1.2 pore volumes was plotted. In Figure 12, the measured MMP indicates that a fully miscible state for the CO_2–oil system can be dynamically established via multiple-contact mechanisms at the original formation pressure.

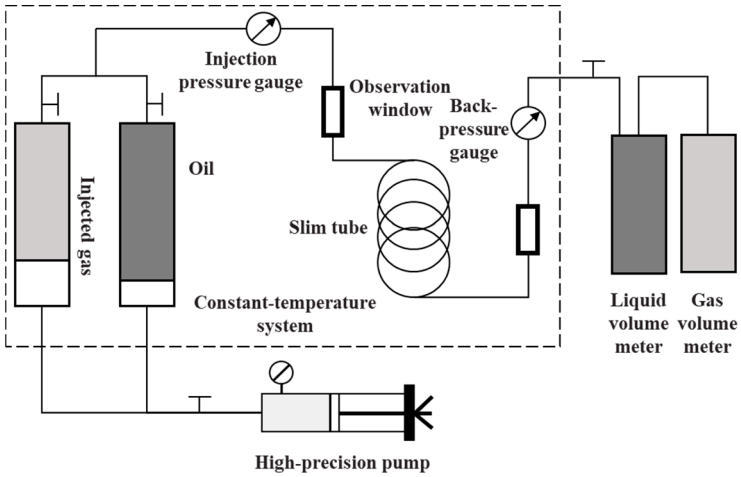


Figure 11. Flow diagram of the slim-tube test.

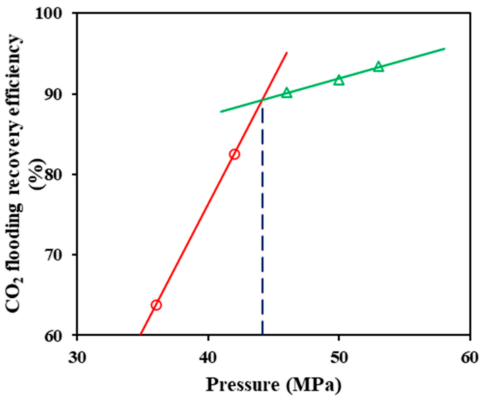


Figure 12. Relationship curve between CO_2 flooding recovery efficiency and displacement pressure in the slim tube test.

4. Miscibility Mechanisms of the CO_2–Oil

4.1. Multiple-Contact Miscibility Mechanisms of the CO_2–Oil

The PR EoS is employed to establish MMC models for the vaporizing, condensing, and vaporizing/condensing gas drives of the CO_2–oil system. Figure 13 calculates the tie-line lengths and equilibrium constants generated by the CO_2 vaporizing gas drive under various pressures. As shown in Figure 13a,b, the tie-line lengths of the crude oil components do not universally decrease with increasing pressure. The tie-line lengths of the intermediate components (C_2–C_6) exhibit a trend of initially decreasing, then increasing, and ultimately experiencing a gradual decrease. This phenomenon occurs because the equilibrium constant of these components equals one at the inflection point. Before the inflection point, the equilibrium constant gradually decreases, and the molar fraction of the vapor-phase component gradually approaches that of the liquid-phase component. At the inflection point, the equilibrium constant equals one, and the theoretical tie-line length of the component is equal to one. Beyond the inflection point, the equilibrium constant drops below one, and the tie-line length begins to increase progressively. These results indicate that the method proposed by some scholars [47,48] (extrapolating the minimum tie-line length) is not universally valid. Utilizing Equation (2) as the criterion is severely misleading; if Equation (2) is used to evaluate this fluid, the calculated MMP would be approximately 3 MPa, which contradicts the experimental measurements. The correct criterion is to sum the lengths of all tie-lines (i.e., summing Equation (2) over all components). When the total tie-line length is zero, the pressure at that point is identified as the MMP. The

MMP calculated using the method proposed in Figure 2 is 45.44 MPa. In Table 5, the calculation results of the proposed model are consistent with those of commercial software, demonstrating an average absolute relative error of 0.81%, thereby verifying the accuracy of the established model.

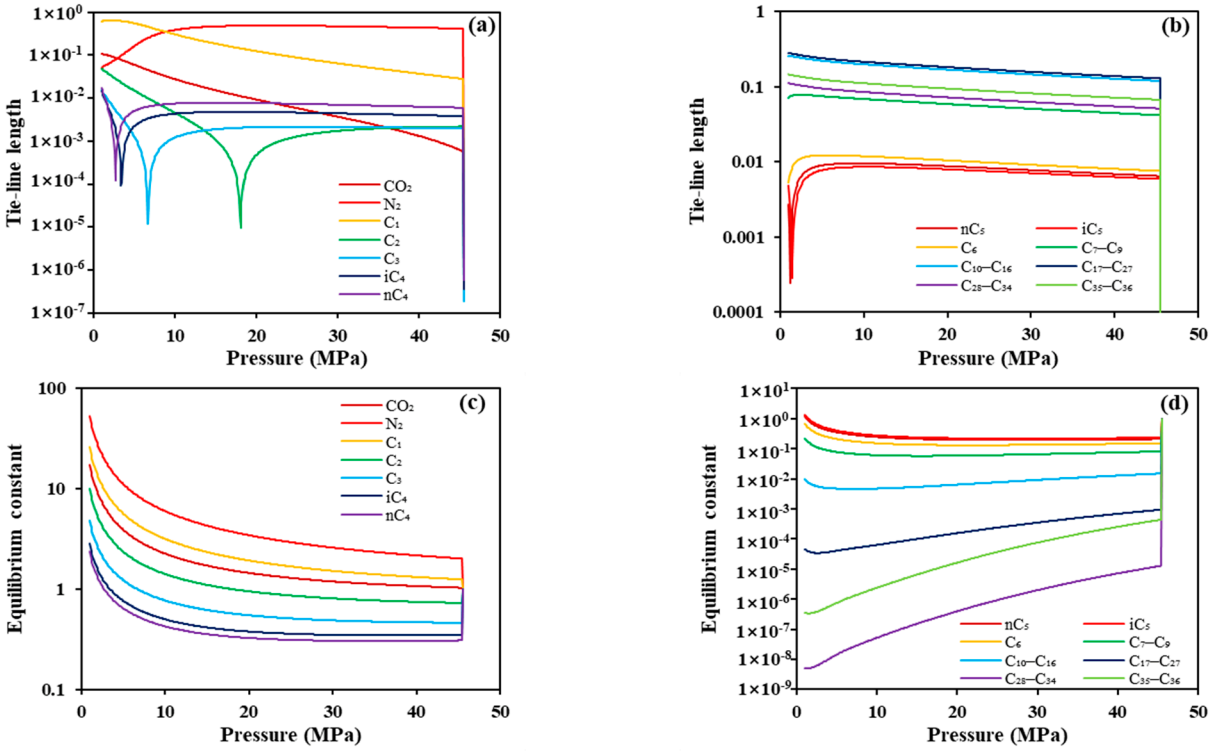


Figure 13. Tie-line lengths of each component vs. pressure (**a**,**b**); equilibrium constants of each component vs. pressure (**c**,**d**) during CO_2 vaporizing gas drive.

Table 5. Calculations of MMP at the different temperatures.

T (°C)	MMC (MPa)	PVTsim [49] (MPa)	Relative Error (%)
130	46.41	45.53	1.93
132	46.06	45.48	1.28
134	45.80	45.45	0.77
136	45.63	45.45	0.40
138	45.52	45.47	0.11
140	45.44	45.51	0.15
142	45.38	45.57	0.42
144	45.33	45.64	0.68
146	45.32	45.73	0.90
148	45.34	45.82	1.05
150	45.35	45.92	1.24

Figure 13 demonstrates that when the pressure reaches the MMP, an abrupt change occurs in the component tie-lines; however, whether CO_2 and the crude oil achieve miscibility can be investigated through the multiple-contact process at pressures before this abrupt change. Figure 14 illustrates the forward multiple-contact process between CO_2 and the crude oil at 140 °C and 45.4 MPa. Initially, the C_{7+} content in the reservoir crude oil exceeds 80%. Following the first contact with CO_2, the C_{7+} content drops to slightly over 40%, whereas the $CO_2 + N_2 + C_1$ content in the crude oil increases from below 20% to nearly 60%, revealing the pronounced solubility of CO_2 within the oleic phase. During the multiple-contact process, the $CO_2 + N_2 + C_1$ content in the liquid phase increases from less

than 60% to nearly 90%. The C_2–C_6 content in the vapor phase remains almost constant, while the C_{7+} content increases to nearly 10%, demonstrating that the significant components extracted by the vapor phase are the heavy C_{7+} components. In the pseudo-ternary phase diagram, the front-end vapor phase and liquid phase eventually merge, indicating that miscibility is achieved after multiple contacts, which further validates the accuracy of the calculated MMP.

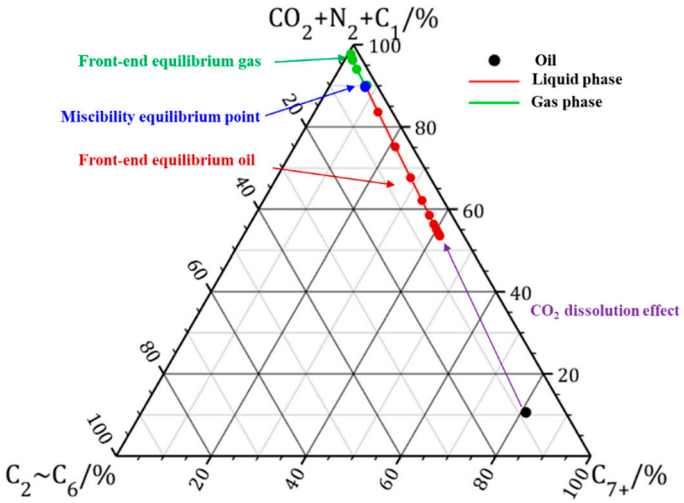


Figure 14. Forward multiple contact pseudo-ternary composition phase diagram (140 °C and 45.4 MPa).

Figure 15 calculates the tie-line lengths and equilibrium constants generated by the CO_2 condensing gas drive under different pressures. As shown in Figure 15a,b, CO_2 continuously extracts N_2 and C_1–C_9 from the crude oil, resulting in only C_{10+} remaining in the liquid phase at the rear-end of the displacement, which may induce asphaltene precipitation. Figure 15 indicates that the MMP of the condensing gas drive is 40.3 MPa.

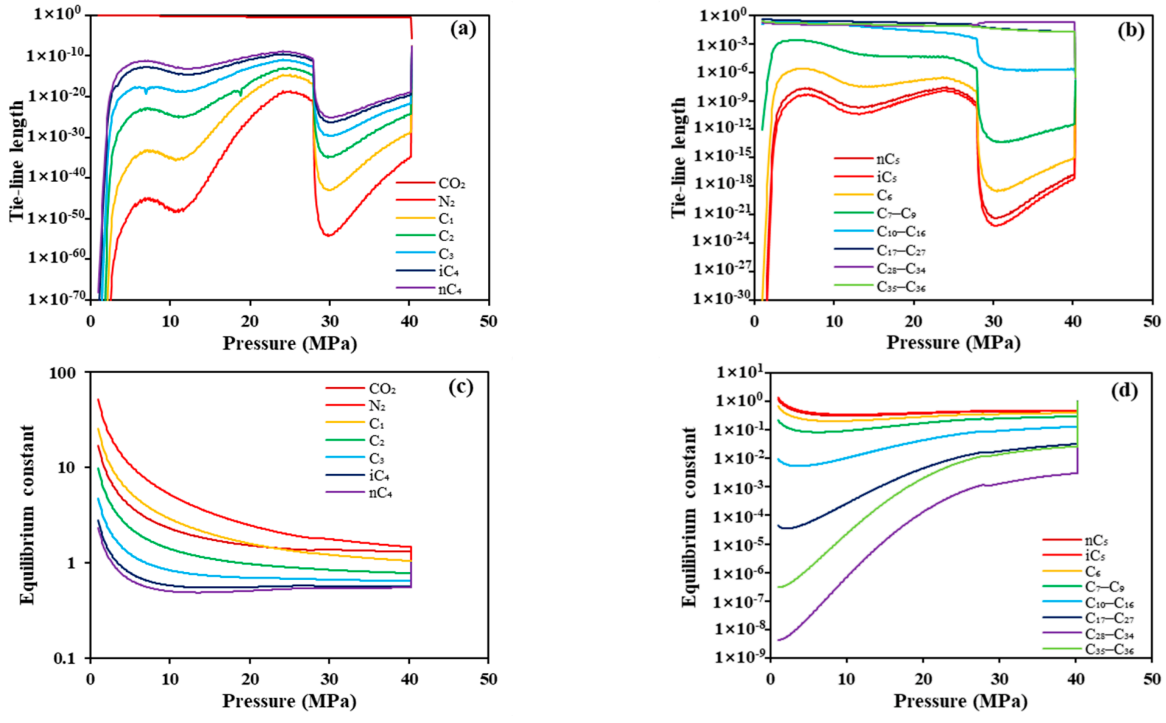


Figure 15. Tie-line lengths of each component vs. pressure (**a**,**b**); equilibrium constants of each component vs. pressure (**c**,**d**) during the CO_2 condensing gas drive.

Figure 16 depicts the backward multiple-contact processes between CO_2 and the crude oil at 140 °C and 40.3 MPa (a) and 40.2 MPa (b). As shown in Figure 16a, at the rear-end of the contact, CO_2 primarily achieves miscibility by dissolving into the liquid phase. The miscibility point is located near the 100% (CO_2 + N_2 + C_1) point, indicating that the post-miscibility phase state is a vapor phase. At 40.2 MPa, the rear-end equilibrium gas moves toward 100% (CO_2 + N_2 + C_1), whereas the rear-end equilibrium oil moves toward 76% (CO_2 + N_2 + C_1) + 24% (C_{7+}). The equilibrium vapor and liquid phases migrate in opposite directions, signifying that miscibility cannot be achieved at this pressure. The pseudo-ternary composition analysis of the backward multiple-contact process rules out the condensing gas drive as the governing miscibility mechanism.

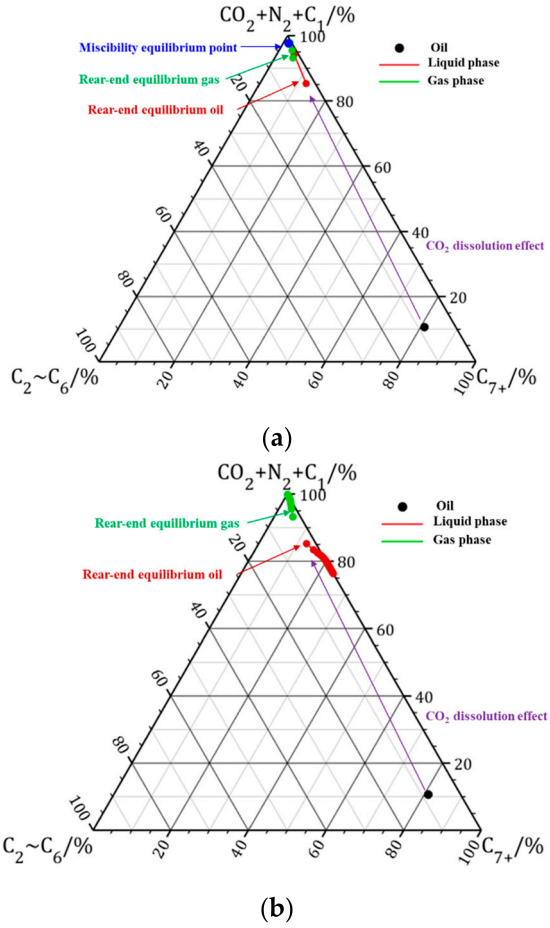


Figure 16. Backward multiple contact pseudo-ternary composition phase diagram: (**a**) 40.3 MPa and (**b**) 40.2 MPa.

Figure 17 calculates the tie-line lengths and equilibrium constants generated by the combined CO_2 vaporizing/condensing gas drive under various pressures. A comparison with Figures 13 and 15 reveals that the tie-line lengths in Figure 17 exhibit the characteristics of both the vaporizing gas drive and the condensing gas drive. Figure 17 indicates that the MMP of the combined vaporizing/condensing gas drive is 41.6 MPa, which lies between the MMPs of the vaporizing gas drive and the condensing gas drive.

Figure 18 illustrates the forward and backward multiple-contact processes between CO_2 and the crude oil at 140 °C and 41.5 MPa. As shown in Figure 18 the forward and backward multiple-contact processes consist of a series of tie-lines. The superposition of these multiple tie-lines demonstrates that a miscible state is ultimately reached. As Li et al. [26] pointed out, supercritical CO_2 establishes a dual displacement mechanism during the flooding process, simultaneously forming a front-end vaporizing miscible drive

and a rear-end condensing miscible drive. Considering that the MMP of the vaporizing gas drive (45.44 MPa) > the slim-tube experimental MMP (44.13 MPa) > the MMP of the vaporizing/condensing gas drive (41.6 MPa), the miscibility mechanism between the formation fluid and CO_2 is primarily governed by the vaporizing gas drive.

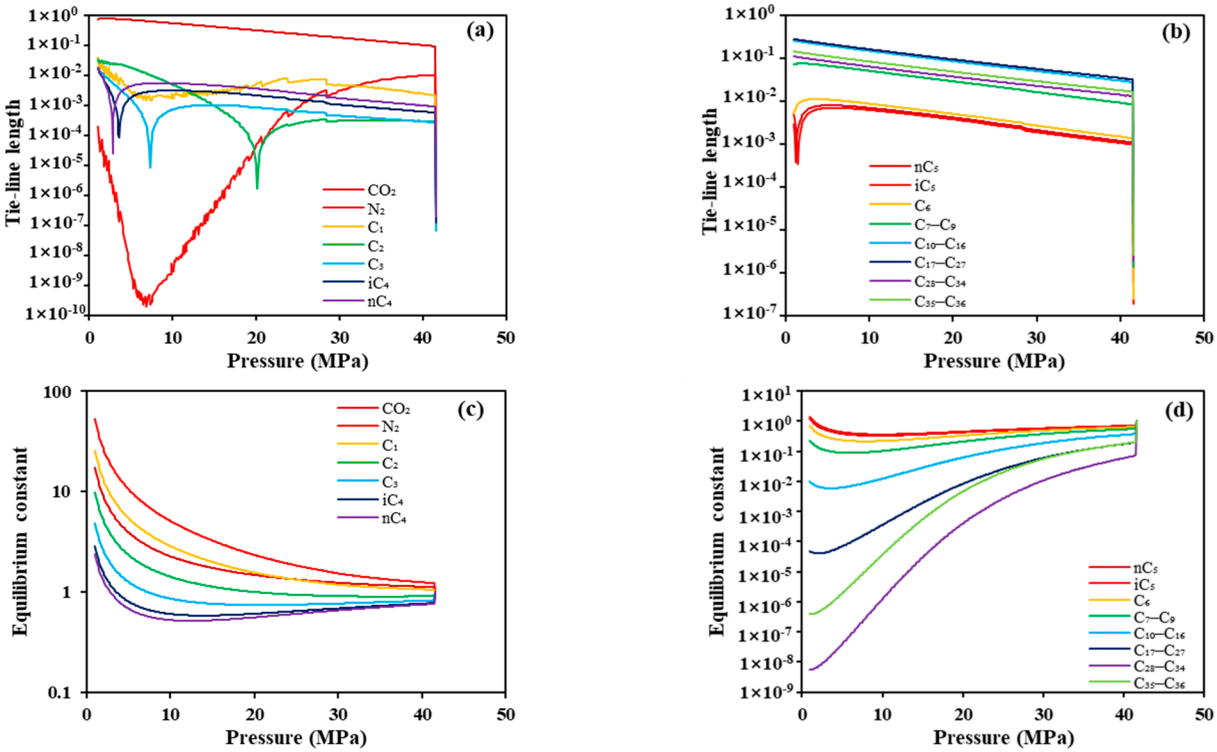


Figure 17. Tie-line lengths of each component vs. pressure (**a**,**b**); equilibrium constants of each component vs. pressure (**c**,**d**) during CO_2 vaporizing/condensing gas drive.

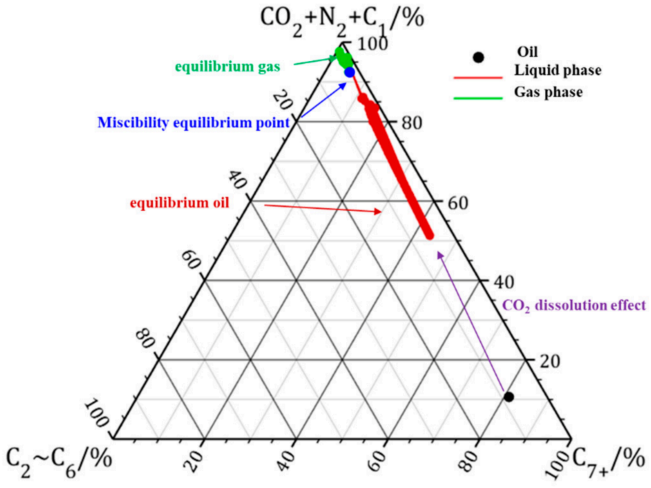


Figure 18. Forward and backward multiple contact pseudo-ternary composition phase diagram (140 °C and 41.5 MPa).

For field-scale CO_2 flooding, this vaporizing-dominated mechanism implies that injection pressure should be maintained close to or above the slim-tube MMP and that sufficient contact length and contact time are required for CO_2 to extract C_{7+} fractions and enrich the oil phase with light components. Condensing mass transfer may still occur at the rear of the displacement path, but the present phase-behavior results indicate that condensing drive alone is unlikely to control miscibility in this HTHP medium–oil system.

4.2. Prediction of the CO_2–Oil MMP Using the MOC

The MOC is employed to predict the CO_2–oil MMP. The component configurations of the key tie-lines for the 15-component system are presented in Table 6. Figure 19 illustrates the variations in different key tie-lines with pressure. When the pressure reaches 39 MPa, the lengths of multiple crossover tie-lines decrease to zero; hence, this pressure is determined to be the MMP. Compared with the slim-tube MMP of 44.13 MPa, the MOC result is lower by 11.62%. This deviation is not only caused by mathematical simplification, but also by the phase-behavior characteristics of this specific HTHP fluid. The crude oil contains a large C_{7+} fraction and exhibits strong CO_2 dissolution and heavy-component extraction during multiple contacts. The MOC assumes one-dimensional, isothermal, dispersion-free equilibrium flow, negligible capillary and gravity effects, negligible pressure-gradient variation, and constant volume during interphase mass transfer. These assumptions shorten the calculated key tie-lines and allow crossover tie-lines to reach zero length earlier than in the experimental multiple-contact displacement. Therefore, the MOC is useful for rapid trend screening, but it is less reliable for heavy-component HTHP oils where vaporizing and condensing mass-transfer paths evolve simultaneously.

Table 6. Component structure of the key tie-line for a 15-component system.

Key Tie-Line	N_2	CO_2	C_1	C_2	C_3	iC_4	nC_4	iC_5	nC_5	C_6	C_7–C_9	C_{10}–C_{16}	C_{17}–C_{27}	C_{28}–C_{34}	C_{35}–C_{36}
Oil tie-line	√	√	√	√	√	√	√	√	√	√	√	√	√	√	√
Crossover tie-line 1		√	√	√	√	√	√	√	√	√	√	√	√	√	√
Crossover tie-line 2		√		√	√	√	√	√	√	√	√	√	√	√	√
Crossover tie-line 3		√			√	√	√	√	√	√	√	√	√	√	√
Crossover tie-line 4		√				√	√	√	√	√	√	√	√	√	√
Crossover tie-line 5		√					√	√	√	√	√	√	√	√	√
Crossover tie-line 6		√						√	√	√	√	√	√	√	√
Crossover tie-line 7		√							√	√	√	√	√	√	√
Crossover tie-line 8		√								√	√	√	√	√	√
Crossover tie-line 9		√									√	√	√	√	√
Crossover tie-line 10		√										√	√	√	√
Crossover tie-line 11		√											√	√	√
Crossover tie-line 12		√												√	√
Injected gas tie-line		√													√

Note: "√" indicates that the component is included in the corresponding key tie-line, whereas a blank cell indicates that the component is absent or not considered in that tie-line.

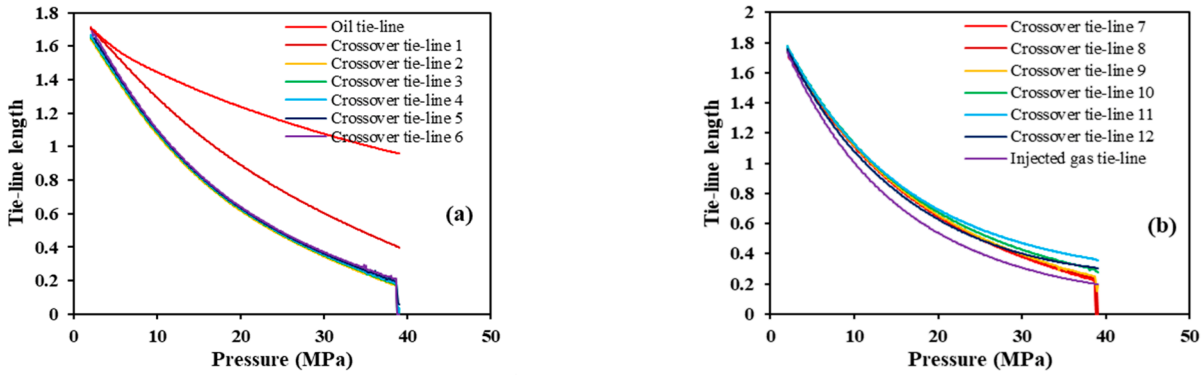


Figure 19. Key line length as a function of pressure: (**a**) oil tie-line and crossover tie-lines 1–6; (**b**) crossover tie-lines 7–12 and injected gas tie-line.

4.3. Prediction of the CO_2–Oil MMP Using Numerical Simulation

The numerical model employed in this study is detailed in Refs. [35,36]. The slim tube is simplified into a one-dimensional Cartesian model with a length, width, and height of 10 m, 0.005 m, and 0.005 m, respectively. The grid is arranged along the axial flow direction, with the transverse directions represented by single cells to maintain the one-dimensional slim-tube displacement assumption. The slim tube is assumed to be homogeneous, with a

permeability of 1 D and a porosity of 0.3. The experimentally measured gas–oil relative permeability curves are applied (Figure 20a). CO_2 is injected from the left boundary until the injected volume reaches 1.2 PV; the right boundary is produced at constant pressure equal to the initial pressure, and the lateral boundaries are treated as no-flow boundaries. For each pressure case, the calculation is continued until oil recovery after 1.2 PV injection is stable with further time-step refinement. In Figure 20b, the MMP obtained via numerical simulation is 46 MPa.

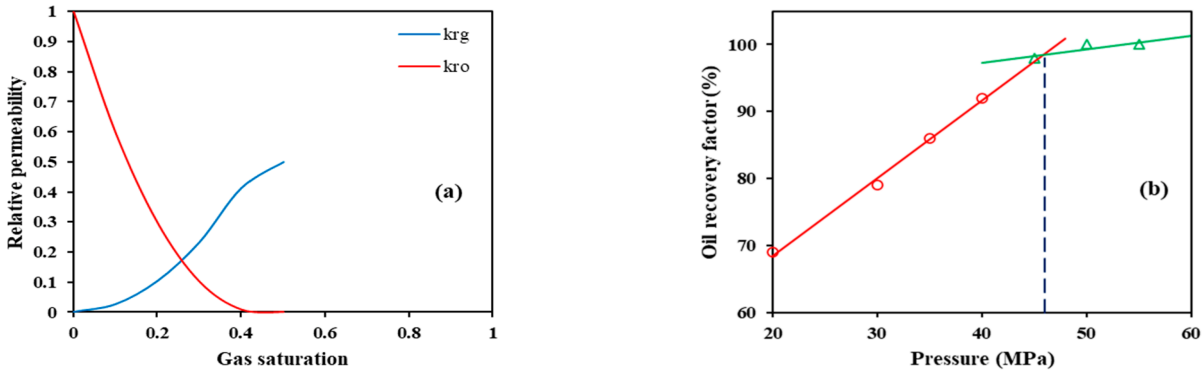


Figure 20. Gas–oil relative permeability curve (**a**); recovery degree vs. pressure (**b**).

4.4. Prediction of the CO_2–Oil MMP Using Intelligent Algorithms

The dataset used for intelligent-model development consists of 31 records, including 20 literature and experimental records summarized in Table 1 (including the present slim-tube experiment) and 11 HTHP calculated records from Table 5. The input variables are reservoir temperature, gas-composition descriptors (x_{vol} and x_{int}), and heavy-fraction molecular-weight descriptors (MWC_{5+} and MWC_{7+}), while the output variable is MMP. The dataset is divided into training, validation, and test subsets in a 7:2:1 proportion, with cross-validation applied during model development and parameter selection. To avoid circular validation, MMC-calculated HTHP records are used only to broaden the HTHP input domain and test model consistency; agreement with MMC or PVTsim is not treated as independent experimental proof of model accuracy. Model accuracy is evaluated primarily against measured MMP values from the literature and the present slim-tube experiment. The population size of the wolf pack is set to 100, and the maximum number of iterations is fixed at 200. The key parameters of the RBF, LSSVM, and SVM models are systematically optimized; the resulting optimized parameters are summarized in Table 7.

Table 7. Parameter values of the three models after optimization.

GWO-RBF			GWO-LSSVM		GWO-SVM		
Target Error	**Smoothness**	**Number of Neurons**	**Penalty Parameter**	**Kernel Parameter**	**Loss Function *c* Value**	**Kernel Function Parameter**	**Loss Function *p*-Value**
0.00025	8.45	55	530.55	0.69	−1.067	−0.0041	−10

Figure 21a compares the predicted values of the various models against the experimental data. The three intelligent algorithms show acceptable predictive performance within the compiled data domain, whereas the empirical correlation proposed by Li et al. [23] fails to accurately predict the CO_2–oil MMP under HTHP conditions. The average absolute relative errors (AARE) for the GWO-RBF, GWO-LSSVM, GWO-SVM, and empirical correlation are 4.22%, 2.58%, 4.67%, and 11.89%, respectively. Figure 21b displays the outlier detection results for the different models. Although a single outlier is identified in both

the GWO-LSSVM and GWO-SVM models, all other data points reside within the reliable domain, substantiating the robustness of the three intelligent models within the available data range.

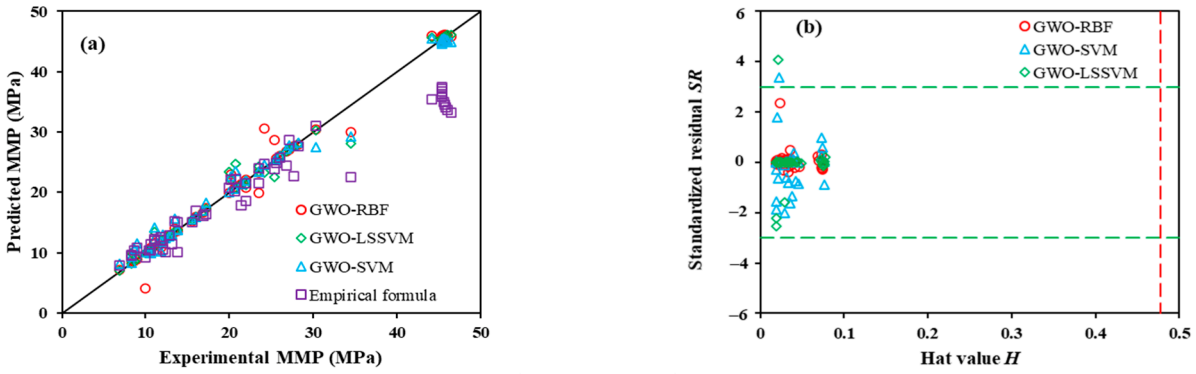


Figure 21. MMP predictions vs. experimental data (**a**); MMP outlier detection (**b**).

Table 8 details the MMP predictions generated by the different models. A comparison with the commercial PVTsim software (version 3.0.367, Calsep A/S, Kongens Lyngby, Denmark) reveals that the MMC, GWO-RBF, GWO-LSSVM, and GWO-SVM results are generally consistent with the thermodynamic benchmark, whereas the MOC and empirical correlation methods yield larger deviations. When benchmarked against the MMP measured via the slim-tube experiment at 140 °C, the MMC method achieves the highest accuracy (2.97% deviation), followed successively by GWO-SVM (3.08%), GWO-LSSVM (3.40%), numerical simulation (4.24%), GWO-RBF (4.26%), MOC (11.62%), and the empirical correlation (19.74%). For additional statistical validation of the HTHP predictions in Table 8, the MAE/RMSE values are 0.499/0.557 MPa for GWO-RBF, 0.388/0.440 MPa for GWO-LSSVM, and 0.390/0.552 MPa for GWO-SVM. Mechanistically, MMC performs best because it explicitly simulates vaporizing, condensing, and combined multiple-contact paths using calibrated phase behavior. Numerical simulation additionally incorporates flow and relative permeability effects, but it is sensitive to grid design and boundary conditions. MOC and empirical correlations are efficient screening tools, but their simplified assumptions make them less suitable for heavy-component HTHP oil systems. Intelligent algorithms can provide supplementary predictions when the input domain is covered by training data; however, their generalization capability remains limited by the scarcity of independent HTHP experimental MMP data.

Table 8. Predictions of the MMP of different models.

T (°C)	MMC (MPa)	MOC (MPa)	GWO-RBF (MPa)	GWO-LSSVM (MPa)	GWO-SVM (MPa)	Empirical Formula (MPa)	PVTsim (MPa)
130	46.41	34.90	45.85	46.12	44.95	33.28	45.53
132	46.06	35.80	45.99	46.04	45.17	33.71	45.48
134	45.80	36.60	46.07	45.94	45.33	34.14	45.45
136	45.63	37.40	46.10	45.84	45.44	34.57	45.45
138	45.52	38.10	46.08	45.73	45.49	34.99	45.47
140	45.44	39.00	46.01	45.63	45.49	35.42	45.51
142	45.38	39.60	45.89	45.54	45.43	35.84	45.57
144	45.33	40.60	45.71	45.45	45.31	36.26	45.64
146	45.32	41.40	45.49	45.36	45.14	36.68	45.73
148	45.34	42.00	45.21	45.28	44.92	37.10	45.82
150	45.35	42.60	44.88	45.19	44.65	37.52	45.92

5. Limitations and Future Work

Several limitations should be noted. First, the experimental validation is based on one representative deep-to-ultra-deep HTHP reservoir fluid; additional independent HTHP slim-tube datasets are needed to improve the generalization of intelligent models. Second, no core-flooding experiment was performed in this study, so core size, core permeability, heterogeneity, and rock-fluid interaction effects were not evaluated [50]. Third, because the experiments focus on CO_2–oil phase behavior, the potential effects of acidic CO_2-brine-rock reactions on mineral dissolution, porosity, permeability, and wettability were not quantified; related studies on high-temperature water/gas sources, CO_2-brine-carbonate reactions, and ultrahigh-pressure pore-structure changes indicate that these coupled thermal-fluid-geochemical effects deserve separate investigation [1,51,52]. Fourth, only the PR EoS calibrated by available PVT data was used for the main calculations; future work should compare PR, SRK, CPA/eCPA, electrolyte-association, and other association-type EoS models under HTHP conditions. Future research will therefore combine independent HTHP experimental datasets, core-flooding validation, EoS sensitivity analysis, geochemical reaction evaluation, and field-scale uncertainty quantification to improve the reliability of CO_2 miscible flooding design.

6. Conclusions

This study provides an integrated experimental, thermodynamic, numerical, and data-driven evaluation of CO_2–oil MMP and miscibility mechanisms for a deep HTHP oil reservoir. The main scientific contribution is not only the measured MMP value, but also the clarification that the high-MMP behavior of this medium–oil system is controlled by pressure-dependent CO_2 dissolution, heavy-component extraction, and vaporizing-dominated multiple-contact miscibility. The conclusions are as follows:

1. When the injected CO_2 mole fraction exceeds 0.88, the formation crude oil and CO_2 remain in a two-phase state at any pressure. Therefore, the crude oil and CO_2 cannot achieve first-contact miscibility. However, 0.12 mol of crude oil can dissolve a maximum of 0.88 mol of CO_2 (oil:CO_2 = 1:7.3 mol/mol) when the reservoir pressure exceeds 52.1 MPa.
2. Supercritical CO_2 establishes a dual displacement mechanism during the flooding process, simultaneously forming a front-end vaporizing miscible drive and a rear-end condensing miscible drive. Considering that the MMP of the vaporizing gas drive (45.44 MPa) > the slim-tube experimental MMP (44.13 MPa) > the MMP of the vaporizing/condensing gas drive (41.6 MPa), the miscibility mechanism between the formation fluid and CO_2 is primarily governed by the vaporizing gas drive.
3. During the vaporizing gas drive process, a substantial amount of CO_2 can dissolve into the crude oil. The CO_2 + N_2 + C_1 content in the liquid phase increases from less than 60% to nearly 90%. The C_2–C_6 content in the vapor phase remains almost unchanged, whereas the C_{7+} content increases to nearly 10%, indicating that the heavy C_{7+} fractions are the significant components extracted by the vapor phase.
4. The MMC method yields the highest predictive accuracy for the MMP, followed successively by the GWO-SVM, GWO-LSSVM, numerical simulation method, GWO-RBF, MOC, and empirical formula. The predicted average absolute relative deviations are 2.97%, 3.08%, 3.40%, 4.24%, 4.26%, 11.62%, and 19.74%, respectively.

Supplementary Materials: The following supporting information can be downloaded at: https://www.mdpi.com/article/10.3390/pr14132073/s1. References [53–55] are cited in the Supplementary Materials.

Author Contributions: Conceptualization, H.-M.W.; methodology, W.X.; validation, L.-J.L.; formal analysis, W.X. and Y.T.; investigation, H.-M.W. and H.C.; resources, Y.-J.Z.; data curation, Y.T. and Y.-J.Z.; writing—original draft preparation, X.-Y.J.; writing—review and editing, X.-Y.J.; supervision, Y.-L.Z.; project administration, Y.-L.Z.; funding acquisition, Y.-L.Z. All authors have read and agreed to the published version of the manuscript.

Funding: This research was funded by the National Science and Technology Major Project (No. 2024ZD1406601), the Sichuan Science and Technology Program (No. 2026NSFSCZY0001, No. 2025ZNSFSC1355), National Natural Science Foundation of China (No. U23A2022, No. 52234003, No. 52474047).

Data Availability Statement: The data presented in this study are available on request from the corresponding author.

Conflicts of Interest: Authors Hong-Mei Wang, Li-Jian Li, Hong Chen, and Yu-Jia Zeng were employed by the PetroChina Huabei Oilfield Company. The remaining authors declare that the research was conducted in the absence of any commercial or financial relationships that could be construed as potential conflicts of interest.

References

1. Zhang, G.H.; Xie, Z.Z.; Zhang, B.W.; Jiao, Y.Y.; Zou, J.P.; Wu, J.Q.; Xiong, F.; Tang, Z.C. Sources of high-temperature water and gas inrush during tunnel excavation: A case of Bangfu tunnel in Southwest China. *J. Rock Mech. Geotech. Eng.* **2024**, *16*, 5027–5049. [CrossRef]
2. Holm, L.W.; Josendal, V.A. Mechanisms of oil displacement by carbon dioxide. *J. Pet. Technol.* **1974**, *26*, 1427–1438. [CrossRef]
3. Alston, R.B.; Kokolis, G.P.; James, C.F. CO_2 minimum miscibility pressure: A correlation for impure CO_2 streams and live oil systems. *Soc. Pet. Eng. J.* **1985**, *25*, 268–274. [CrossRef]
4. Rathmell, J.J.; Stalkup, F.I.; Hassinger, R.C. A laboratory investigation of miscible displacement by carbon dioxide. In *Proceedings of the SPE Annual Technical Conference and Exhibition, New Orleans, LA, USA, 3 October 1971*; SPE: Richardson, TX, USA, 1971; p. SPE–3483-MS. [CrossRef]
5. Jaubert, J.N.; Avaullee, L.; Souvay, J.F. A crude oil data bank containing more than 5000 PVT and gas injection data. *J. Pet. Sci. Eng.* **2002**, *34*, 65–107. [CrossRef]
6. Zuo, Y.X.; Chu, J.Z.; Ke, S.L.; Guo, T.M. A study on the minimum miscibility pressure for miscible flooding systems. *J. Pet. Sci. Eng.* **1993**, *8*, 315–328. [CrossRef]
7. Eakin, B.E.; Mitch, F.J. Measurement and correlation of miscibility pressures of reservoir oils. In *Proceedings of the SPE Annual Technical Conference and Exhibition, Houston, TX, USA, 2 October 1988*; SPE: Richardson, TX, USA, 1988; p. SPE–18065-MS. [CrossRef]
8. Sun, Y.H.; Lü, G.Z.; Wang, Y.F. A method of state equation for determining minimum miscible pressure of CO_2. *Pet. Geol. Recovery Effic.* **2006**, *13*, 82–84. (In Chinese)
9. Graue, D.J.; Zana, E.T. Study of a possible CO_2 flood in Rangely Field. *J. Pet. Technol.* **1981**, *33*, 1312–1318. [CrossRef]
10. Dicharry, R.M.; Perryman, T.L.; Ronquille, J.D. Evaluation and design of a CO_2 miscible flood project-SACROC unit, Kelly-Snyder field. *J. Pet. Technol.* **1973**, *25*, 1309–1318. [CrossRef]
11. Gardner, J.W.; Orr, F.M.; Patel, P.D. The effect of phase behavior on CO_2-flood displacement efficiency. *J. Pet. Technol.* **1981**, *33*, 2067–2081. [CrossRef]
12. Thakur, G.C.; Lin, C.J.; Patel, Y.R. CO_2 minitest, Little Knife Field, ND: A case history. In *Proceedings of the SPE Improved Oil Recovery Conference, Tulsa, OK, USA, 15 April 1984*; SPE: Richardson, TX, USA, 1984; p. SPE–12704-MS. [CrossRef]
13. Metcalfe, R.S. Effects of impurities on minimum miscibility pressures and minimum enrichment levels for CO_2 and rich-gas displacements. *SPE J.* **1982**, *22*, 219–225. [CrossRef]
14. Dong, M.; Huang, S.; Dyer, S.B.; Mourits, F.M. A comparison of CO_2 minimum miscibility pressure determinations for Weyburn crude oil. *J. Pet. Sci. Eng.* **2001**, *31*, 13–22. [CrossRef]
15. Shelton, J.L.; Yarborough, L. Multiple phase behavior in porous media during CO_2 or rich-gas flooding. *J. Pet. Technol.* **1977**, *29*, 1171–1178. [CrossRef]
16. Henry, R.L.; Metcalfe, R.S. Multiple-phase generation during carbon dioxide flooding. *SPE J.* **1983**, *23*, 595–601. [CrossRef]
17. Khan, S.A.; Pope, G.A.; Sepehrnoori, K. Fluid characterization of three-phase CO_2/oil mixtures. In *Proceedings of the SPE Improved Oil Recovery Conference, Tulsa, OK, USA, 22 April 1992*; SPE: Richardson, TX, USA, 1992; p. SPE–24130-MS. [CrossRef]
18. Chaback, J.J.; Harmon, R.A.; Grigg, R.B. Discussion of vapor-density measurement for estimating minimum miscibility pressure. *SPE Reserv. Eng.* **1989**, *4*, 253–254.

19. Spence, A.P., Jr.; Watkins, R.W. The effect of microscopic core heterogeneity on miscible flood residual oil saturation. In *Proceedings of the SPE Annual Technical Conference and Exhibition, Dallas, TX, USA, 21 September 1980*; SPE: Richardson, TX, USA, 1980; p. SPE–9229-MS. [CrossRef]
20. Al-Ajmi, M.; Alomair, O.; Elsharkawy, A. Planning miscibility tests and gas injection projects for four major Kuwaiti reservoirs. In *Proceedings of the SPE Kuwait International Petroleum Conference and Exhibition, Kuwait City, Kuwait, 14 December 2009*; SPE: Richardson, TX, USA, 2009; p. SPE–127537-MS. [CrossRef]
21. Cronquist, C. Carbon dioxide dynamic miscibility with light reservoir oils. In Proceedings of the 4th Annual U.S. DOE Symposium, Tulsa, OK, USA, 28–30 August 1977.
22. Lee, K.H.; Lombardo, M.; Sandler, S.I. The generalized van der Waals partition function. II. Application to the square-well fluid. *Fluid Phase Equilibria* **1985**, *21*, 177–196. [CrossRef]
23. Li, H.; Qin, J.; Yang, D. An improved CO_2-oil minimum miscibility pressure correlation for live and dead crude oils. *Ind. Eng. Chem. Res.* **2012**, *51*, 3516–3523. [CrossRef]
24. Li, J.; Li, S. A new method to forecast the CO_2-oil minimum miscibility pressure based on multicontact curve. *Pet. Geol. Recovery Effic.* **2014**, *21*, 51–54.
25. Tang, Y.; Sun, L.; Li, S.L.; Guo, P.; Li, Y.G. On evaluation of miscible gas-flooding mechanism. *Xinjiang Pet. Geol.* **2004**, *4*, 414–417. (In Chinese)
26. Li, S.L.; Sun, L.; Chen, Z.H.; Li, J.; Tang, Y.; Pan, Y. Further discussion on reservoir engineering concept and development mode of CO_2 flooding-EOR technology. *Reserv. Eval. Dev.* **2020**, *10*, 1–14. (In Chinese)
27. Yang, X.F.; Guo, P.; Du, Z.M. Calculate minimum miscibility pressure. *Nat. Gas Ind.* **2004**, *6*, 98–102. (In Chinese)
28. Tian, X.F.; Tan, X.H.; Zhang, L.J.; Yang, X.G.; Jiao, Y.J.; Ling, H.C.; Zhang, L.; Han, D. Study on factors affecting minimum miscibility pressure of CO_2 flooding by tie-line analysis. *Reserv. Eval. Dev.* **2019**, *9*, 32–35. (In Chinese)
29. Wang, Q.F. Review on determine methods of minimum miscibility phase pressure of CO_2 miscible flooding. *Chem. Ind. Eng. Prog.* **2011**, *30*, 805–808. (In Chinese)
30. Shen, B.; Yang, S.L. Prediction model of minimum miscible pressure of CO_2-crude oil based on PSO-GBDT. *Sci. Technol. Eng.* **2022**, *22*, 7866–7872. (In Chinese)
31. Shao, G.Q.; Guo, P.; Wu, L.; Wang, Z.H.; Fan, J.W.; Liu, H.; Sun, B.W.; Wen, B. The influence of slim tube length on the minimum miscibility pressure of hydrocarbon gas-crude oil and the improved prediction model. *Sci. Technol. Eng.* **2020**, *20*, 11548–11554. (In Chinese)
32. Luo, Z.S.; Zhang, J.Q.; Luo, J.H.; Wang, X.W. Prediction of minimum miscibility pressure for CO2 flooding based on the IMA-AmMLP model. *Acta Pet. Sin.* **2024**, *45*, 1522–1528. (In Chinese)
33. Peng, D.Y.; Robinson, D.B. A new two-constant equation of state. *Ind. Eng. Chem. Fundam.* **1976**, *15*, 59–64. [CrossRef]
34. Wang, Y.; Orr, F.M., Jr. Analytical calculation of minimum miscibility pressure. *Fluid Phase Equilibria* **1997**, *139*, 101–124. [CrossRef]
35. Xiong, W.; Zhao, Y.L.; Wen, S.M.; Zhang, B.N.; Huang, X.; Wang, Y.C.; Zhang, T. Influence of diffusion, adsorption, connate water, and salinity on enhanced gas recovery and carbon storage reservoir simulations. *Energy Fuels* **2024**, *38*, 12645–12657. [CrossRef]
36. Xiong, W.; Zhang, L.H.; Zhao, Y.L.; Wen, S.M.; Bao, K.; Møyner, O.; Lie, K.A. Compositional simulation for carbon storage in porous media using an electrolyte association equation of state. *SPE J.* **2024**, *29*, 3314–3336. [CrossRef]
37. Xiong, W.; Zhang, L.H.; Zhao, Y.L.; Wu, J.F.; Huang, J.H.; Yao, J. A generalized equation of state for associating fluids in nanopores: Application to CO_2-H_2O, CH_4-H_2O, CO_2-CH_4, and CO_2-CH_4-H_2O systems and implication for extracting dissolved CH4 by CO2 injection. *Chem. Eng. Sci.* **2021**, *229*, 116034. [CrossRef]
38. Xiong, W.; Zhang, L.H.; Tian, Y.; Li, L.X.; Zhao, Y.L.; Chen, Z.X. Phase equilibrium modeling for carbon dioxide capture and storage (CCS) fluids in brine using an electrolyte association equation of state. *Chem. Eng. Sci.* **2023**, *275*, 118723. [CrossRef]
39. Xiong, W.; Zhang, L.H.; Zhao, Y.L.; Wen, S.M.; Liu, L.L.; Cao, Z.L.; Wang, Y.C.; Luo, S.G.; Jiang, X.Y. Phase equilibrium modeling for CCUS fluids using a modified association equation of state. *J. Supercrit. Fluids* **2025**, *219*, 106543. [CrossRef]
40. Soave, G. Equilibrium constants from a modified Redlich-Kwong equation of state. *Chem. Eng. Sci.* **1972**, *27*, 1197–1203. [CrossRef]
41. Park, J.; Sandberg, I.W. Universal approximation using radial-basis-function networks. *Neural Comput.* **1991**, *3*, 246–257. [CrossRef] [PubMed]
42. Cortes, C.; Vapnik, V. Support-vector networks. *Mach. Learn.* **1995**, *20*, 273–297. [CrossRef]
43. Mirjalili, S.; Mirjalili, S.M.; Lewis, A. Grey wolf optimizer. *Adv. Eng. Softw.* **2014**, *69*, 46–61. [CrossRef]
44. *GB/T 26981-2020*; Analysis Method for Physical Properties of Reservoir Fluids. State Administration for Market Regulation and Standardization Administration of the People's Republic of China: Beijing, China, 2020. (In Chinese)
45. Computer Modelling Group Ltd. *CMG WINPROP User's Guide*, Version 2021; Computer Modelling Group Ltd.: Calgary, AB, Canada, 2021.
46. *SY/T 5542-2009*; Analysis Method for Physical Properties of Reservoir Fluids. Beijing COC Tech Co., Ltd.: Beijing, China, 2009. (In Chinese)

47. Zhang, C.S.; Fan, Z.F.; Xu, A.Z. An effective way to forecast minimum miscibility pressure based on improved multiple-mixing-cell approach. *Fault-Block Oil Gas Field* **2016**, *23*, 606–609. (In Chinese)
48. Tian, Z. Research on the Calculation of Minimum Miscibility Pressure Based on Tie-Line Analysis Method. Master's Thesis, China University of Petroleum (Beijing), Beijing, China, 2022. (In Chinese)
49. Calsep. *PVTsim Nova*, Version 7.2; Calsep: Kongens Lyngby, Denmark, 2024.
50. Sun, M.D.; Duan, X.G.; Liu, Q.; Blach, T.P.; Ostadhassan, M.; Liu, B.; Ji, Y.P.; Hu, Q.H.; Pan, Z.J. The importance of pore-fracture connectivity in overmature marine shale for methane occurrence and transportation. *Mar. Pet. Geol.* **2023**, *157*, 106495. [CrossRef]
51. Zhao, Y.L.; Wang, Y.C.; Wen, S.M.; Zhang, L.H.; Cao, Z.L.; Zhao, Z.H.; Xiong, W.; Cao, C.; Tang, R.; Fan, Y.T. In-situ experiments of dynamic microscopic reaction for CO2-brine-carbonate system. *Chem. Eng. J.* **2025**, *506*, 160251. [CrossRef]
52. Ma, X.M.; Wen, P.C.; Fan, Y.P.; Dong, X.S.; Sun, W.; Min, F.F.; Feng, Z.Y.; Xie, J.G. Quantitative analysis of high-efficiency dewatering under ultrahigh pressures: Moisture storage state and filter-cake pore structure. *Miner. Eng.* **2026**, *237*, 109969. [CrossRef]
53. Jiao, Z.; Gao, S.; Liu, C.; Luo, J.; Wang, Z.; Lang, G.; Zhao, Z.; Wu, Z.; He, C. Digital Model of Plan View Pattern Control for Plate Mills Based on Machine Vision and the DBO-RBF Algorithm. *Metals* **2024**, *14*, 94. [CrossRef]
54. Burges, C.J.C. A Tutorial on Support Vector Machines for Pattern Recognition. *Data Min. Knowl. Discov.* **1998**, *2*, 121–167. [CrossRef]
55. Suykens, J.A.K.; Vandewalle, J. Least Squares Support Vector Machine Classifiers. *Neural Process. Lett.* **1999**, *9*, 293–300. [CrossRef]

Disclaimer/Publisher's Note: The statements, opinions and data contained in all publications are solely those of the individual author(s) and contributor(s) and not of MDPI and/or the editor(s). MDPI and/or the editor(s) disclaim responsibility for any injury to people or property resulting from any ideas, methods, instructions or products referred to in the content.